Latest progress in Hall thrusters plasma modelling

F. Taccogna, Laurent Garrigues

Latest progress in Hall thrusters plasma modelling

F. Taccogna, Laurent Garrigues

Reviews of Modern Plasma Physics (2019) …

https://doi.org/.... [1]

REVIEW PAPER

Latest Progress in Hall Thrusters Plasma Modelling

F. Taccogna[1] L. Garrigues[2]

Received: ? / Accepted: ?

Abstract

In the last thirty years, numerical models have revealed different physical mechanisms involved in the Hall thruster functioning leading to a bridge between analytical prediction / empirical intuition and experiments. For this reason, modeling effort is continuously increasing in the domain of Hall Thrusters. Two basic approaches exist: one based on fluid/hybrid simulation where the distribution of electrons is assumed Maxwellian and the plasma inside the thruster, considered as quasineutral, is described with macroscopic quantities (density, velocity and energy); the second approach is based on kinetic description for charged particles where no approximation is made for the distribution of particles.

Fluid or hybrid approaches offer the advantage of demanding low run times and computational resources. They are very useful to perform parametric studies but actually the anomalous phenomena responsible for electron transport across the magnetic field barrier have not been self-consistently modeled. Kinetic approach is able to better capture phenomena originating on the Debye scale length like the lateral sheaths, ExB electron drift instability, important to explain the anomalous electron transport, but it requires very long run times. For this latter, the progress in computer science offers the advantage to describe conditions more and more close to the thruster operation.

In this review, we will present the two approaches emphasizing on numerical schemes used with assumptions and approximations and on main results obtained. Future directions on the Hall thruster modeling will finally outlined.

Keywords Hall Thruster · Particle-in-Cell · Plasma sheath · Secondary electron emission · Electron cyclotron drift instability

F. Taccogna
francesco.taccogna@cnr.it
Extended author information available on the last page of the article

Published online: ?

1 Introduction

To move and/or control the motion of satellites around Earth's orbit or spacecrafts for Space trips, a propulsion system must be used to achieve the mission by exerting a force called thrust under the ejection of matter (action-reaction principle). The success of electric propulsion utilization is based on the ability to eject a high-speed propellant and mass economy induced at launch to realize such missions. For a large overview and state-of-art of the electric propulsion topic, the reader can refer to textbooks of Jahn (2006), Turner (2009), Goebel and Katz (2008), to review articles of Ahedo (2011), Garrigues and Coche (2011), Mazouffre (2016), Levchenko et al. (2018), and to recent special issues of IEEE Transactions on Plasma Sciences, vol. 43(1) (2015) and Plasma Sources Science and Technology, vol. 27 (2018).

Robert Jahn defining the electric propulsion as the acceleration of gases for propulsion by electrical heating and/or electric and magnetic body forces, electrical thrusters have been classified in three main categories.

- Electrothermal thrusters are based on same principles than chemical thrusters where the thrust is the result of a hot gas expansion through a nozzle used to convert thermal energy to kinetic energy, expect that gas heating is achieved through the means of an arc (arcjet) or a resistance (electrojet).

- In electromagnetic thrusters, a propellant gas is ionized. The thrust is produced by the acceleration of charged particles under the Lorentz force that is a combination of applied electric and self-induced magnetic fields resulting from a high discharge current maintained in the plasma.

- Electrostatic thrusters are also based on the ionization of a propellant gas but the thrust is the result of the acceleration of positive ions by an imposed direct-current electric field. Injection of electrons ensured by a neutralizer is necessary to maintain a zero net-current beam. Gridded ion engines are one of the oldest electrostatic thrusters. It consists of two separate stages, an ionization chamber where the plasma is generated by means of direct-current with multipole magnetic field ring-cusp (Kaufman-type source), radio-frequency or microwave fields, and an acceleration stage with a system of polarized grids to accelerate ions at the desired velocity. The main drawback of such engine is due to space charge formed upstream of the grid system that acts as a limiting factor in term of the ion current density extracted and thrust by units of surface (Child-Langmuir law). New missions for electric propulsion, requiring one unique type of engines to be able to ensure high thrust level during orbit transfer, cannot be currently achieved with compact gridded ion engines.

A particular concept of electrostatic propulsion is represented by Hall Thruster (HT). It is based on the application of a magnetic field barrier perpendicular to the direction of the discharge current. In such a way, the electron conductivity locally drops leading to the penetration of the direct-current electric field within the plasma (Boeuf 2017). The axial electric field resulting from the potential drop between anode and cathode electrodes serves to ignite and maintain the plasma by heating electrons and to accelerate ions to furnish the thrust, without space charge limitation. The discharge takes place inside a coaxial channel made in ceramics, generally a boron-nitride with silica compounds, BN-SiO_2 (see Figs. 1 for a schematic and the operations of a 20 kW-class engine). From now on we will always use the cylindrical coordinate system to indicate the various directions The gas propellant (usually heavy noble gases) is impeded at the rear of the channel, through a metallic anode plane. An external cathode serves as electron source whose current is split in two: one fraction corresponding to ~ 20 % of the discharge current is going inward of the channel and after being heated by the electric field ionizes the neutral gas, the rest neutralizes the ion beam ejected from the channel. The discharge current at the anode (~ 4A for a kW-class Hall thruster) is carried by electrons coming from the external cathode source and resulting from the multiplication

in the channel during the gas ionization (fixing the ion current strength produced). The magnetic field whose direction is mainly radial and strength maximum at the exhaust of the channel is established thanks to a system of inner and outer coils and a magnetic circuit made in iron-based materials. The magnetic field strength ~ 100 G is chosen to only confine electrons keeping ions un-magnetized. A Hall current in the azimuthal E×B direction is not interrupted because of the cylindrical symmetry increasing the residence time of the electrons inside the channel giving rise to ionize ~ 90 % of the neutral flux injected. The name of the thruster comes from the azimuthal Hall electron current, while the name of closed electron drift thruster is preferred in the Russian literature.

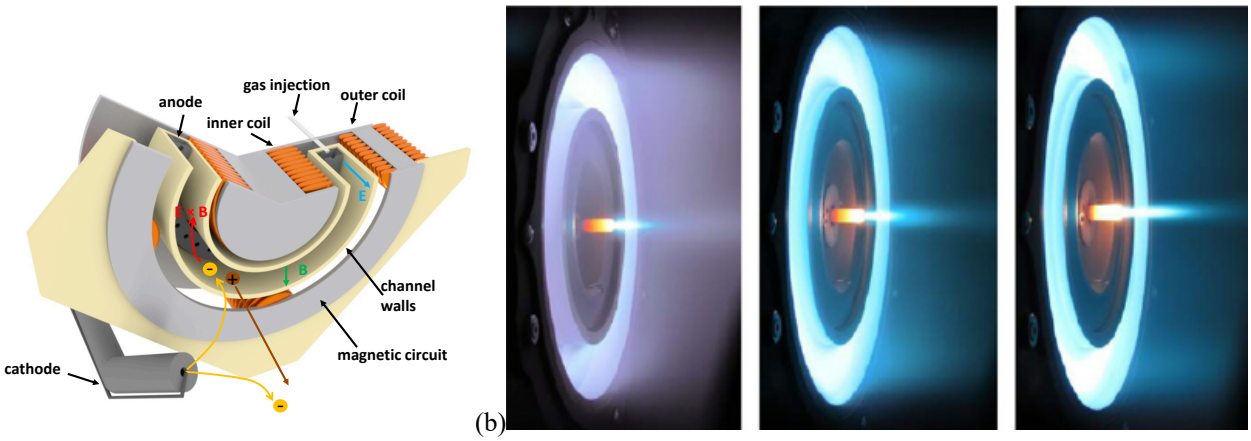

Fig. 1 (a) Schematic of Hall thruster, (b) PPS®-20K ML mounted with the centered cathode operating at different power levels (photo credit: Safran-Snecma).

This review paper is focused on the modeling of HTs and is split in two main parts.

In Sect. 2, fluid/hybrid-based models and main features of the thruster discharge obtained with are detailed. Supported by the existence of an electric field penetrating inside the bulk plasma, the modeling of sheaths becomes un-essential (and can be treated analytically separately), and the hypothesis of quasi-neutrality is appropriated. It offers the advantage of not resolving Debye length and plasma frequency alleviating constraints on timestep and grid-spacing. Low computational cost makes possible parametric studies about the influence of magnetic field, discharge voltage and mass flow rate on thruster operation. In Sect. 2.1, fundamental equations are recalled and their implementations in the context of HT especially for the fluid treatment of strongly magnetized electrons are depicted. Sect. 2.2 is focused on the method to obtain the electric potential profile in quasi-neutral models and the encountered difficulties linked to an almost free transport of electrons along magnetic field lines contrary to the resistive cross-magnetic field transport. Analytical sheaths including secondary electron emission (SEE) under high-energy electron impacts on ceramic walls are treated in Sect. 2.3. The role of non-collisional phenomena that controls cross-magnetic field transport of electrons is crucial and cannot be captured in fluid/hybrid-based models for the simple reason that the azimuthal direction that is the siege of field fluctuations and induced transport is not described (see Sect. 3). Anomalous electron collision frequencies using empirical laws have consequently been introduced in electron transport equations (the different phenomena invoked are gathered in Sect. 2.4). Quantitative information about anomalous transport can also been extracted from measurements. An attempt to extract information from fully kinetic PIC simulations to self-consistently capture anomalous transport through the resolution of a wave equation is also discussed in Sect. 2.4. Even if fluid/hybrid models are not fully predictive, almost qualitatively, they are able to explain the complex operation of HTs, this is illustrated in the rest of that part. Sec. 2.5 gives a clear understanding of the thruster working and how the overlap between ionization and

acceleration regions are responsible for channel wall erosion and reduced thruster lifespan. Different operating regimes and the role of the type of ceramics are highlighted in Sect. 2.6. In Sect. 2.7, one example of utilization of fluid/hybrid-based models to predict channel wall erosion is detailed. One objective is to increase thruster lifetime and one possible way is to reduce radial electric field and sheath potential drop close to channel exhaust. After back and forth between simulations and experiments and after a deep analysis of plasma properties, one magnetic field topology called magnetic shielded configuration has been proposed and validated, this is detailed in Sect. 2.8.

Sect. 3 deals with the kinetic treatment of electrons. It is a fundamental aspect of HTs due to weak collisionality, anisotropy and strong SEE from the two lateral walls. The deviation from the equilibrium distribution can have an important impact on macroscopic quantities, like ionization efficiency, wall losses and transport coefficients. It can also drives microscopic instabilities leading to fluctuations in all the three directions at the expense of a thruster efficiency reduction. In Sect. 3.1 the models based on the direct solution of the electron Boltzmann equation will be presented. They shows the importance of the ExB configuration and electron-wall interaction. From Sect. 3.2 to Sect. 3.5 the different fully kinetic Particle-in-Cell (PIC) models developed for HTs will discussed. Sect. 3.2 presents one-dimensional radial models focusing on the importance of the lateral sheath regimes, electron-wall interaction and cylindrical geometry on the plasma dynamics in the acceleration region of the HT discharge channel. Sect. 3.3 presents the extension of radial models to include the axial coordinate. This leads to 2D axisymmetric models that give a quite complete representation (some time including also part of the plume region) of the HT functioning. Due to this completeness this class of models are often used to investigate particular magnetic field configuration and to assess the ion wall erosion. The plasma behavior along the azimuthal direction is presented in Sect. 3.4 where one-dimensional and the two two-dimensional (in combination with the axial and radial direction, respectively) models are presented. All results obtained have highlighted the importance of ExB drift instability to induce azimuthal fluctuations but also the limitation of low-dimensional models and the strong coupling among the different coordinates. The few fully kinetic three-dimensional attempts have finally been reported in Sect. 3.5. Kinetic effects can also be important in the plume region and in particular in the region close to the HT exit plane. Sect. 3.6 deals with some numerical approaches able to handle this problem. Finally, Sect. 3.7 is dedicated to the presentation of zero-dimensional kinetic models, such as global and collisional-radiative models. Summary and final evaluations and suggestions are reported in Sect. 4.

2 Fluid/hybrid models of channel and near field regions

In this section we focus on fluid/hybrid models of Hall thrusters and its applications to model the thruster operations.

2.1 Principles of fluid and hybrid approaches

Different types of models have been developed, starting from one-dimensional model along the axial direction inside the channel in the late 1990s, with an extension to the near field region where the magnetic field is still large, in the following years. At the same time, one-dimensional models along the radial direction have been used to simulate the effect of SEE under the impact of high-energy electrons on ceramic walls of the channel on plasma properties. Two-dimensional models that account for axial and radial directions most of time including channel and near field regions have been developed at the beginning of 2000s to better capture plasma properties and expansion. More recently, a two-dimensional model along the axial and azimuthal directions has been proposed. A list of models is given Tab. I. Developed models are fully fluid or hybrid when electrons are treated as a fluid and heavy species (ions and neutrals) with a kinetic description.

Authors/References	Model type	SEE	Transient	Electric Potential	Regions
Boeuf and Garrigues (1998)	1D (z) hybrid	No	Yes	QN	Channel
Ashkenazy et al. (1999)	1D (z) hybrid	No	No	QN	Channel
Morozov and Savelyev (2000a)	1D (z) hybrid	No	Yes	QN	Channel
Keidar et al. (2001)	1D (r) fluid	Yes	No	Poisson	Channel
Ahedo et al. (2002)	1D (z) hybrid	No	No	QN	Channel/ Near field
Roy and Pandey (2002)	1D (z) fluid	Yes	Yes	QN	Channel
Ahedo (2002)	1D (r) fluid	Yes	No	Poisson	Channel
Ahedo et al. (2003)	1D (z) hybrid	Yes	No	QN	Channel/ Near field
Barral et al. (2003)	1D (z) fluid	Yes	Yes	QN	Channel
Hara et al. (2012)	1D (z) hybrid	No	No	QN	Channel
Komurasaki and Arakawa (1995)	2D (z,r) hybrid	No	No	QN	Channel
Fife (1998)	2D (z,r) hybrid	Yes	Yes	QN	Channel/ Near field
Hagelaar et al. (2002)	2D (z,r) hybrid	No	Yes	QN	Channel/ Near field
Koo and Boyd (2004)	2D (z,r) hybrid	No	Yes	QN	Channel/ Near field
Keidar et al. (2004)	2D (z,r) fluid	No	No	QN	Channel
Parra et al. (2006)	2D (z,r) hybrid	Yes	Yes	QN	Channel/ Near field
Garrigues et al. (2006)	2D (z,r) hybrid	Yes	Yes	QN	Channel/ Near field
Mikellides and Katz (2012)	2D (z,r) fluid	Yes	Yes	QN	Channel/ Near field
Lam et al. (2015)	2D (z,θ) hybrid	Yes	Yes	QN	Channel/ Near field
Andreussi et al. (2018)	2D (z,r) fluid	Yes	Yes	QN	Channel/ Near field

Tab. I 1D and 2D fluid/hybrid models of HTs by chronological order. QN is used for quasi-neutral assumption.

Fluid description of particles

Each species of mass m is characterized by a distribution function $f(\mathbf{r},\mathbf{v},t)$ that is a solution of the Boltzmann equation:

$$\frac{\partial f}{dt} + \mathbf{v}.\frac{\partial f}{d\mathbf{r}} + \frac{\mathbf{F}}{m}.\frac{\partial f}{d\mathbf{v}} = \left\{\frac{\partial f}{dt}\right\}_c, \quad (1)$$

where $\mathbf{F}$ is the force and the right-hand side term is the collisional term. The properties of species are described by macroscopic quantities obtained by averaging the distribution function of particles f over the velocity space. The quantities depending on space $\mathbf{r}$ and time t are density n, mean velocity $\mathbf{u}$ and mean energy ε:

$$n = \int f(\mathbf{r},\mathbf{v},t)d^3\mathbf{v}, \quad (2)$$

$$\mathbf{u} = \bar{\mathbf{v}} = \frac{1}{n}\int \mathbf{v}f(\mathbf{r},\mathbf{v},t)d^3\mathbf{v}, \quad (3)$$

$$\varepsilon = \frac{m}{2e}\overline{v^2} = \frac{m}{2en}\int v^2 f(\mathbf{r},\mathbf{v},t)d^3\mathbf{v}\ . \quad (4)$$

In the rest of this section, we will consider a plasma made of electrons, singly charged ions, and neutral atoms using subscripts e, i, and a, in equations, respectively. We focus on established equations in the context of HT modelling.

The density n is the solution of continuity equation that is obtained by integration of Eq. (1) over velocity space:

$$\frac{\partial n}{\partial t} + \nabla.(n\mathbf{u}) = S_{\mathrm{v}} + S_{\mathrm{w}}\,, \qquad (5)$$

where S_{v} and S_{w} are the sources of particles generated or lost in volume and on walls after recombination of ions, respectively. In HTs, electropositive gases are employed and only binary collisions occur. The plasma density is small enough to neglect recombination between charged particles. The mechanism responsible of charged particles production (and neutral atom losses) is the ionization of neutrals (and ions when stepwise ionization is included) by electrons:

$$S_{\mathrm{v}} = \sum_j R_j, \qquad (6)$$

where $R_j = k_j n_{1,j} n_{2,j}$ is the number of particles created (or lost) for one type of reaction that depends on densities of the colliding particles and of the reaction rate $k_j = \langle \sigma_j v_r \rangle$, σ_j corresponds to the ionization cross section, v_r the relative velocity (modulus) between species (that can be reduced to electron velocity) and the brackets indicates an average over the distribution function of electrons. Assuming a Maxwellian distribution leads to tabulate the ionization rate as a function of the electron mean energy ε_e. In one dimensional models of Tab. I, only single charged ions were considered, while more recent simulations of HT operations include multiply charged ions that are produced from direct ionization of xenon ground state and stepwise ionization from ions (Koo et al. 2004; Mikellides and Katz 2012; Garrigues 2016). S_{w} is the result of recombination of ions at a frequency $\nu_{i,\mathrm{w}}$ in neutral atoms at the walls (positive sign for neutrals and negative for ions):

$$S_{\mathrm{w}} = \pm n \nu_{i,\mathrm{w}}. \qquad (7)$$

The recombination frequency $\nu_{\mathrm{w},i}$ is simply:

$$\nu_{i,\mathrm{w}} = \mathrm{A}\frac{\mathrm{v}_{i,\mathrm{w}}}{h}\,, \qquad (8)$$

where A is a constant (~ 0.7-1.2) that accounts for the dynamic of the radial presheath (Ahedo et al. 2003).

The mean velocity $\mathbf{u}$ is obtained after multiplying Eq. (1) by $\mathbf{v}$ and integration over velocity space. Assuming that the tensor of pressure is diagonal and isotropic (for more details, see e.g. Krall and Trivelpiece 1973), and after substitution of Eq. (5), the simplified momentum equation under the general form writes:

$$\frac{\partial \mathbf{u}}{\partial t} + (\mathbf{u}.\nabla)\mathbf{u} = \frac{q}{m}(\mathbf{E} + \mathbf{u} \times \mathbf{B}) - \frac{e}{mn}\nabla(nT) - \nu_m \mathbf{u} - \frac{S_{\mathrm{w}}}{n}\mathbf{u}\,, \qquad (9)$$

where the momentum transfer frequency to particles from other species j is defined as:

$$\nu_m = \sum_j \frac{m_j}{m+m_j} k_{m,j} n_j + \frac{S_{\mathrm{v}}}{n}. \qquad (10)$$

In Eq. (9), the mean target velocity $\mathbf{u}_j$ has been neglected. The left-hand side term are the convective (inertia) terms and time ($\partial\mathbf{u}/\partial t$) and velocity $[(\mathbf{u}.\nabla)\mathbf{u}]$ variations. The right-hand terms corresponds to forces acting on particles under the effects of electric and magnetic fields (that vanishes for neutrals), gradient of pressure ($P = enT$, where T is the temperature and e the elementary charge), collisions (including ionization) in volume, and wall effects for heavy species.

For electrons, neglecting inertia terms and heavy species velocity during collisions, and after rearranging and with $T_e = 2\varepsilon_e/3$, Eq. (9) can be written as:

$$n_e\mathbf{u}_e + \mathbf{\Omega}_e \times (n_e\mathbf{u}_e) = -\frac{e}{m_e\nu_e}n_e\mathbf{E} - \frac{2}{3}\frac{e}{m_e\nu_e}\nabla(n_e\varepsilon_e) = -\mu_0 n_e\mathbf{E} - \frac{2}{3}\mu_0\nabla(n_e\varepsilon_e), \quad (11)$$

where $\mathbf{\Omega}_e$ is the Hall parameter (vector) that indicates how much electrons are magnetized:

$$\mathbf{\Omega}_e = e\mathbf{B}/m_e\nu_e, \quad (12)$$

and $\mu_0 = e/m_e\nu_e$ is the mobility coefficient for non-magnetized electrons (mobility parallel to the magnetic field). Rearranging Eq. (11), it is convenient to express the electron flux $\mathbf{\Gamma}_e$ under the drift-diffusion form:

$$\mathbf{\Gamma}_e = n_e\mathbf{u}_e = -n_e\overline{\overline{\boldsymbol{\mu}_e}}.\mathbf{E} - \frac{2}{3}\overline{\overline{\boldsymbol{\mu}_e}}.\nabla(n_e\varepsilon_e). \quad (13)$$

In Eq. (13), $\overline{\overline{\boldsymbol{\mu}_e}}$ is the mobility tensor, with anisotropic diagonal components $\mu_\parallel = \mu_0$ parallel to $\mathbf{B}$, $\mu_\perp = \mu_0/(1+\Omega^2)$ normal to $\mathbf{B}$, and non-diagonal term $\mu_x = \pm\mu_0\Omega/(1+\Omega^2)$ in the $\mathbf{E}\times\mathbf{B}$ direction, (Hagelaar et al. 2011). In the momentum transfer frequency ν_e, electron-atom and electron-ion collisions are included, as well as other phenomena responsible for the so-called anomalous transport (see Sect. 2.4).

The situation is different for ions, since $\Omega_i \gg L$ (length of the channel), ions are not magnetized and inertia terms are no longer negligible. In the collision term, charge exchange (backscattering) and isotropic collisions between ions and neutrals and Coulomb collisions have been included (Mikellides and Katz 2012). Recombination of ions at the walls can be considered according to Eq. (7). Finally, the pressure term is either neglected considering cold ions (Andreussi et al. 2018) either simplified considering a specified ion temperature (Mikellides and Katz 2012).

In most of fluid/hybrid simulations of HTs, momentum and electron energy equations for neutral atoms are not solved but a constant velocity of neutrals $\mathbf{v}_a$ is assumed leading to obtain the profile of neutral density n_a solving Eq. (5). This has been done in one-dimensional models of (Boeuf and Garrigues 1998, Morozov and Savelyev 2000a, Ahedo et al. 2002). Barral et al. (2003) have considered two populations of neutral atoms and two equations of continuity: the first one inferred to neutrals injected through the orifice at a given temperature and the second population in equilibrium with the (fixed) wall temperature. Eq. (5) has been modified accordingly. In the two-dimensional fluid model, Mikellides and Katz (2012) have proposed a specific algorithm to calculate the distribution function of neutral and moments of neutral transport from Eqs. (2-4).

The energy equation is only solved for electrons. The electron mean energy ε_e is obtained after multiplying Eq. (1) by $mv_e^2/2$ and integration over velocity space:

$$\frac{\partial(en_e\varepsilon_e)}{\partial t} + \nabla.(en_e\varepsilon_e\mathbf{u}_e + \mathbf{P}_e.\mathbf{u}_e + \mathbf{Q}_e) = -en_e\mathbf{u}_e.\mathbf{E} - \mathrm{C}_{e,\mathrm{v}} - \mathrm{C}_{e,\mathrm{w}}, \quad (14)$$

where $C_{e,v}$ and $C_{e,w}$ are the power losses by electrons in collisions and on the walls, respectively, and $\mathbf{Q}_e$ is the electron flux vector that is assumed proportional to the gradient of temperature (to close the system, see Bittencourt 2004):

$$\mathbf{Q}_e = -\overline{\overline{\boldsymbol{\kappa}}}\nabla\varepsilon_e = -\frac{10}{9}\nabla.\left(en_e\varepsilon_e\overline{\overline{\boldsymbol{\mu}_e}}.\nabla\varepsilon_e\right). \qquad (15)$$

Remark that due to magnetic field, the thermal conductivity is anisotropic. Assuming that the directed energy ($mu_e^2/2\,e$) is smaller than the thermal energy ($3T_e/2$), Eq. (14) becomes:

$$\frac{\partial(n_e\varepsilon_e)}{\partial t} + \frac{5}{3}\nabla.n_e\mathbf{u}_e\varepsilon_e - \frac{10}{9}\nabla.\left(n_e\varepsilon_e\overline{\overline{\boldsymbol{\mu}_e}}.\nabla\varepsilon_e\right) = -n_e\mathbf{u}_e.\mathbf{E} - \frac{1}{e}C_{e,v} - \frac{1}{e}C_{e,w}. \quad (16).$$

It is convenient to separate the term $C_{e,v}$ in two contributions, the first one due to inelastic processes (excitation and ionization) and a second one due associated to momentum transfer (Hagelaar et al. 2011). The term $C_{e,w}$ is also addressed in Hagelaar et al. (2011). Boeuf and Garrigues (1998) have solved Eq. (15) neglecting the thermal flux and assuming a stationary solution. Barral et al. (2003) have considered a possible anisotropy of electron mean energy and two independents stationary energy equations parallel and perpendicular to the magnetic field. Only the two-dimensional models cited in Tab. I do solve Eq. (15) in its complete form.

Direct kinetic / Particle-in-Cell (PIC) description of heavy species

In kinetic description of heavy species no assumption is made on energy distribution functions and Eq. (1) is solved. A Direct kinetic method with a simple upwind scheme is used by Boeuf and Garrigues (1998) but found a numerical broadening of energy distributions compared to Monte Carlo techniques. Hara et al. (2012) propose an improved numerical scheme to reduce numerical dissipation. The others hybrid models of Tab. I are based on the resolution of Eq. (1) using Particle-in-Cell (PIC) simulations (Hockney-Eastwood 1989 and Birdsall-Langdon 2005), where the energy distribution of heavy species is sampled with a fixed number of macroparticle. Calculations are subject to statistical fluctuations depending on the number of particles used (in hybrid models of HT, a statistic of around 100 particles per cell is enough to capture the heavy species properties, gradient of density, losses on walls, thrust calculation, etc.). In two dimensional (r,z) models ions are defined by their position and velocity (three components). During the ion PIC cycle, the electric field (ions are not sensitive to the magnetic field) is calculated on a grid (see next Sect. 2.2) and the ion equations of motion then integrated in time by interpolating the electric field from the grid nodes to the ion location. The same weighting scheme is also used to calculate heavy species properties (densities and fluxes) on the grid nodes from ion positions. At the end of the ion push, a test is made to determine if the ion positions are still or not in the computational domain. Ions impinging the walls of the channel are neutralized and new neutrals return back in the computational domain (accommodation methods are most often used).

Neutral particles are introduced in the simulation domain through the anode plane at z=0 and uniformly between two fixed radii. The number of injected particles is proportional to the injected mass flow $\dot{m}$ and time step Δt, and inversely proportional to the neutral mass. The initial velocity is sampled from a half-Maxwellian distribution along the z direction at a given injection temperature. After neutrals advance, positions of particles according to computational domain frontiers are checked. Neutrals colliding with walls are isotropically reflected according to half-Maxwellian distribution at the surface temperature in the direction normal to it. Neutrals crossing the open Cartesian boundary beyond the cathode line are eliminated. To simulate vacuum chamber and backpressure effects, a supplementary injection of neutrals at the external frontiers is often used. Between two consecutive time-steps, ionization of the neutral atoms with losses of neutrals and generation of ions must be considered. Standard Monte Carlo Collision or refined Direct Monte

Carlo Simulation (Taccogna 2015) procedures are used. In two-dimensional models, ion species actually taken into account are singly (xenon ground state to first level of ionization) and multiply charged ions (from ground state and stepwise ionization from lower level of ionized atoms). Collisional processes (mainly charge exchange and elastic collisions) between heavy species are most of time considered.

2.2 Quasi-neutrality assumption and electric potential calculation

In HTs, for typical plasma conditions, with a maximum of electron density and temperature on the order of 10^{18} m^{-3} and 50 eV, respectively, the Debye length in the range of 50 μm is much smaller than typical size of the thruster (~ 2 cm). Resolving the Debye length would require a large number of grid points (more than 400 cells in each direction), while this is not essential since the electric field penetrates inside the plasma due to the drop of conductivity. In all the one-dimensional (along the axial coordinate z) and two-dimensional models of Tab. I, the plasma is assumed quasi-neutral and sheaths (including SEE) are described through an analytical approach (see next Sect. 2.3).

The plasma density n_p is:

$$n_p = n_e = \sum_s z_s n_{i,s}, \quad (17)$$

where the sum is taken on all the ion species s of charge state z_s. The electric potential is no longer computed from Poisson's equation but from the electron momentum equation coupled with the current conservation equation. Writing that the electric field derives from the electric potential ($\mathbf{E} = -\nabla\phi$), Eq. (13) becomes:

$$\boldsymbol{\Gamma}_e = n_p \overline{\overline{\boldsymbol{\mu}_e}} . \nabla\phi - \frac{2}{3} \overline{\overline{\boldsymbol{\mu}_e}} . \nabla\left(n_p \varepsilon_e\right) . \quad (18)$$

Substituting the electron and ion fluxes in continuity Eq. (5), it leads to a current continuity equation (generalized Ohm's law) which can be solved to determine the electric potential ϕ:

$$\nabla . \boldsymbol{\Gamma}_e = \nabla . \left[n_p \overline{\overline{\boldsymbol{\mu}_e}} . \nabla\phi - \frac{2}{3} \overline{\overline{\boldsymbol{\mu}_e}} . \nabla\left(n_p \varepsilon_e\right) \right] = \nabla . \boldsymbol{\Gamma}_i, \quad (19)$$

where plasma density and the right term of Eq. (19) are inferred to ion calculation properties. The electron flux involving in Eq. (19) can be expressed in z and r directions as (Hagelaar 2016):

$$\Gamma_{e,z} = n_p \mathrm{u}_{e,z} = \frac{1+\Omega_z^2}{1+\Omega^2} \left[\mu_0 n_p \frac{\partial\phi}{\partial z} - \frac{2}{3} \mu_0 \frac{\partial\left(n_p \varepsilon_e\right)}{\partial z} \right] + \frac{\Omega_z \Omega_r}{1+\Omega^2} \left[\mu_0 n_p \frac{\partial\phi}{\partial r} - \frac{2}{3} \mu_0 \frac{\partial\left(n_p \varepsilon_e\right)}{\partial r} \right] \quad (20.a)$$

$$\Gamma_{e,r} = n_p \mathrm{u}_{e,r} = \frac{1+\Omega_r^2}{1+\Omega^2} \left[\mu_0 n_p \frac{\partial\phi}{\partial r} - \frac{2}{3} \mu_0 \frac{\partial\left(n_p \varepsilon_e\right)}{\partial r} \right] + \frac{\Omega_z \Omega_r}{1+\Omega^2} \left[\mu_0 n_p \frac{\partial\phi}{\partial z} - \frac{2}{3} \mu_0 \frac{\partial\left(n_p \varepsilon_e\right)}{\partial z} \right]. \quad (20.b)$$

The electron flux in each of the directions is the sum of two terms proportional to gradients in longitudinal and transverse directions very large and opposite in sign leading to resolve a five-point elliptic equation strongly anisotropic. Even the use of an accurate numerical scheme able to properly calculate terms separately can fail to resolve the complete system. The consequence is that numerical errors can provide and even become dominant in the electron transport across the magnetic field.

To reduce computational errors, one can solve the same problem but for coordinates aligned and perpendicular to the magnetic field lines (Mikellides and Katz 2012). Such grid, obtained as far as the self-induced magnetic field due to plasma variations is negligible, can be calculated from $\nabla \cdot$

$\mathbf{B} = 0$ and $\nabla \times \mathbf{B} = 0$. Along the magnetic field lines, the magnetic streamlines ψ are obtained from:

$$\frac{\partial \psi}{\partial z} = rB_r, \frac{\partial \psi}{\partial r} = -rB_z, \qquad (21)$$

B_r and B_z being the radial and axial coordinates of magnetic field. The ψ stream function is constant along the magnetic field lines. The construction of the stream function requires a monotonic variation of ψ. This method can also be extended for magnetic topology with a zero-B by considering four different regions in which the stream function presents a monotonic variation (Garrigues et al. 2003). Along the streamline function, a second coordinate χ be defined as:

$$\frac{\partial z}{\partial \chi} = \frac{B_z}{B}, \frac{\partial r}{\partial \chi} = \frac{B_r}{B}. \qquad (22)$$

Any quantities of the system of equations of Sect. 2.1 can be expressed in the direction normal and along the magnetic field lines by:

$$\frac{\partial}{\partial \hat{n}} = rB \frac{\partial}{\partial \psi}, \frac{\partial}{\partial \hat{\beta}} = \frac{\partial}{\partial \chi}. \qquad (23)$$

Functions and typical field-aligned meshes are sketched in Fig. 2.

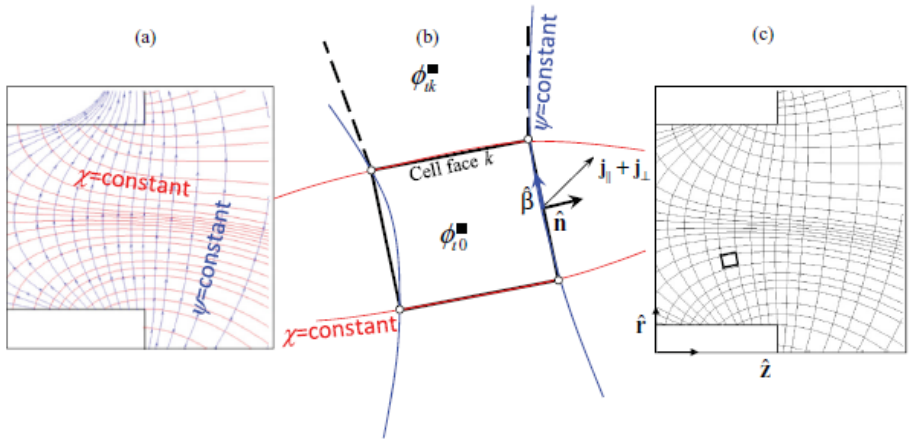

Fig. 2 (a) Constant streamlines Ψ and potential χ functions, (b) each cell face is (closely) aligned with ψ = constant or χ = constant, (c) computational mesh (from Mikellides and Katz 2012).

One can simplify the problem by remarking that along the magnetic field lines, the electron moves freely with a flux limited to ion flux since walls are insulators. The drift and diffusion terms of Eq. (18) compensate each other and the electric potential is given by a Boltzmann's relation:

$$\phi_{\parallel}(z,r) = \frac{2}{3}\varepsilon_e \ln\left[\frac{n_p(z,r)}{n_{p,0}}\right], \qquad (24)$$

where $n_{p,0}$ is a reference plasma density defined at $\phi = 0$. The derivation of Eq. (24) implies that the electron mean energy ε_e is constant along the magnetic field lines. Eq. (19) is then solved in the direction normal to the magnetic field lines on a computational grid in one-dimension defined by the ψ stream function. The electric potential is then written as:

$$\phi(z,r) = \phi^*(\psi) + \frac{2}{3}\varepsilon_e(\psi) \ln\left[\frac{n_p(z,r)}{n_{p,0}}\right], \qquad (25)$$

$\phi^*(\psi)$ is often called "thermalized potential" and Eq. (25) is referred to Morozov's relation (Morozov and Savelyev 2000a)). Accordingly, the electron energy Eq. (16) is also solved in the direction normal to the magnetic field. For typical magnetic field topologies of HTs, calculations with the two-dimensional model (with field-aligned meshes) show that the electric potential is effectively "thermalized" (deviations exist but only in the near field plume close to the cathode (Mikellides and Katz 2012)). Remark that this description leads to avoid any calculations of the electron flux along the magnetic field lines.

2.3 Analytical sheath description including secondary emission electron

The quasi-neutrality assumption leads to describe a separate model of the sheaths. In HTs, the sheath layers, being smaller than any collision mean free paths, are considered collisionless. The positive space charge in front of the surfaces, accelerating ions and repealing electrons, yields to a sheath potential drop that is positive. In the rest of that section, we consider one species of ions (Xe^+) for simplicity.

The establishment of Bohm velocity for ions at the sheath entrance in quasi-neutral model is not automatically achieved, whatever the type of surface. Hybrid calculations of Parra and Ahedo (2004) have shown that the choice in the grid spacing (fine or coarse) affects the gradient of ion density and velocity in the pre-sheath and consequently the ion mean velocity at the wall boundary. Even with a fine mesh, the capability of the quasi-neutral model to satisfy the Bohm sheath criterion is not achieved. One solution is to force the mean velocity normal to the wall being equal to the Bohm velocity, like a boundary condition for fluid models, as done by Mikellides and Katz (2012) in their fluid approach for ions. When ions are treated as particles, Ahedo et al. (2010) have extended previous work of Lampe et al. (1998), proposing a numerical method to force the Bohm velocity at the sheath entrance, also considering more than one ion species.

In the anode plane, since no SEE occurs, for a fluid description of charged particles, one must specify boundary conditions in the direction normal to the surface. For ions, the current density is calculated imposing a Bohm velocity at sheath entrance. For electrons, the current density at anode can be calculated from a Boltzmann distribution for the density and a velocity equal to $\sqrt{8eT_e/\pi m_e}/4$. The energy loss on the surface is $\varepsilon_{e,anode} = 2T_e + \phi_s$, where ϕ_s is the sheath voltage drop. The sheath voltage ϕ_s can be expressed as a function of electron temperature and ion and electron fluxes impeding the anode (Ahedo et al. 2001).

The properties of ceramic walls impose a zero net current. For a flux of electrons $\Gamma_{e,w}$ arriving on the surface and a flux of secondary electrons $\bar{\sigma}\Gamma_{e,w}$ leaving the wall ($\bar{\sigma}$ being defined as the SEE yield σ integrated over a Maxwellian distribution, see Appendix 1), the zero net current imposes:

$$\Gamma_{i,\mathrm{w}} = (1-\bar{\sigma})\Gamma_{e,\mathrm{w}} \,. \quad (26)$$

The presence of secondary electrons induced by high-energy electron impacts on the walls modifies the sheath potential drop (Barral et al. 2003):

$$\phi_s = \mathrm{T}_e \ln\left[(1-\bar{\sigma})\sqrt{\frac{m_i}{2\pi m_e}}\right] . \quad (27)$$

The solution of Eq. (27) is only valid for $\bar{\sigma} < 1$. When $\bar{\sigma} \to 1$, a potential well appears in front of the walls recollecting a fraction of emitted electrons. This so-called space charge saturation (SCS) regime appears when $\bar{\sigma} = \bar{\sigma}_{\mathrm{SCS}} = 1 - 8.3\sqrt{m_e/m_i}$ (Hobbs and Wesson 1967). For Xenon

$\bar{\sigma}_{\mathrm{SCS}} \sim 0.983$, and $\phi_{s,\mathrm{SCS}} \sim \mathrm{T}_e$. In that specific regime, the sheath potential drop is considerably reduced.

Associated to electron-wall interactions, an effective momentum transfer collision frequency involving in Eq. (18) can be calculated (Fife 1998; Barral et al. 2003; Ahedo et al. 2003; Parra et al. 2006, Garrigues et al. 2006). This momentum transfer component acts as a supplementary collision frequency responsible for axial transport of electrons. Including Eq. (26), a qualitative estimation gives:

$$\nu_{e,\mathrm{w}} = \frac{\mathrm{v}_{i,\mathrm{w}}}{h}\frac{\bar{\sigma}}{(1-\bar{\sigma})}, \qquad (28)$$

where $\mathrm{v}_{i,\mathrm{w}}$ is the ion Bohm velocity, $h = R_2 - R_1$ the channel width. The electron power losses associated to SEE (last term right in equation (16)) can also be calculated writing a balance between incoming and outgoing electron energy fluxes (see e.g. Garrigues et al. 2006):

$$\mathrm{C}_{e,\mathrm{w}} = en_eW = en_e\frac{\mathrm{v}_{i,w}}{h}\left\{\frac{4\left(\varepsilon_e-\bar{\sigma}\varepsilon_{e,s}\right)}{3(1-\bar{\sigma})} + \frac{2}{3}\phi_s\right\}, \qquad (29)$$

where $\varepsilon_{e,s}$ is the electron mean energy of electrons emitted that depends on the type of wall materials (Barral et al. 2003).

Previous one-dimensional axial models were using a simplified (rather empirical) effect of the walls on momentum transfer frequency with a constant electron-wall collision frequency ν_{ref} and an electron power loss per second (Boeuf and Garrigues 1998; Hagelaar et al. 2002; Koo and Boyd 2004; Hara et al. 2012) modeled as:

$$W = \alpha_\varepsilon \nu_{\mathrm{ref}} \varepsilon_e \exp(-U/\varepsilon_e), \quad (30)$$

where U is the threshold of SEE. Fig. 3 illustrates the difference between the two approaches, with $\nu_{\mathrm{ref}} = 10^7$ s^{-1}, $\alpha_\varepsilon = 0.7$ and $U = 20$ V and for BN-SiO_2 as ceramic.

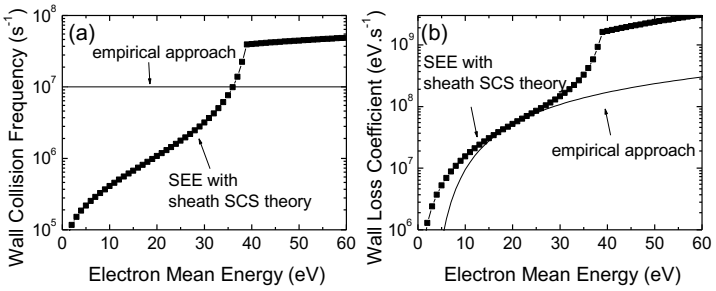

Fig. 3 Comparisons with detailed and empirical approaches to account for electron-wall influence on (a) momentum collision frequency, (b) wall loss coefficient (Garrigues et al. 2006).

2.4 Anomalous electron transport

HT is an $E \times B$ device that confines electrons in the axial direction. To ensure current continuity from cathode to anode, electrons must change momentum in the axial direction of electric field. In the exhaust region, collisions between electrons and heavy species are insufficient to ensure this role since most of neutrals is ionized and under the acceleration of ions, ion density remains too low for Coulomb collisions to affect electron transport. Anomalous transport has been invoked and two different strategies have been adopted. The first one consists in identifying the mechanisms

responsible for an increase of cross-field transport and implant them in fluid equations. Main anomalous transport processes being related to a spatial dimension (azimuthal coordinate) and/or typical scales not considered in most of fluid/hybrid models, cross-B field transport is introduced in fluid equations through an effective collision frequency. The total electron momentum exchange frequency is then written as the sum of the contribution of collisions and anomalous transport, $\nu_e = \nu_{e,\mathrm{coll}} + \nu_{e,\mathrm{ano}}$. Efforts to self-consistently calculate anomalous transport have also recently been proposed. The second approach is purely empirical losing the physical meaning and is based on a cross-B field transport coefficient determined from experimental results.

Inside the channel, electron-wall interactions participate to axial transport making possible for electrons to pass from one confined trajectory to another one upstream closer to the anode (often referred to near-wall conductivity NWC in the literature, see Morozov-Savelyev 2001) enhanced by the SEE (described in Sect. 2.3). In the region of strong magnetic field, plasma turbulence can also play a role. Janes and Lowder (1966) have shown that an anomalous diffusion due to a fluctuating azimuthal electric field E_θ correlated with plasma density variations produce a drift in the $E_\theta \times B_r$ (axial) direction. They found that the Hall parameter remains constant and consequently an effective collision frequency that varies as $k_{\mathrm{ano}}\omega_e$ has been derived. This mechanism has been correlated to Bohm's diffusion (for which $k_{\mathrm{ano}} = 1/16$) and the HT literature often refers to "Bohm's like transport". Based on instabilities suppression or reduction in the region of shear flows in strongly magnetized plasmas (e.g. in Tokamaks, Hahm 2002), Scharfe et al. (2008) have derived a model for the anomalous electron conductivity and have deduced an anomalous collision frequency. Later, Cappelli et al. (2015) by analogy with neutral fluid dynamic have proposed to link anomalous transport to a turbulent viscosity frequency $\nu_{turb} = \gamma \rho_e \mathrm{v}_e$, where ρ_e is the electron Larmor radius, v_e the electron mean velocity and γ a coefficient expected to be on the order of one (but that can be determined experimentally). Two-dimensional PIC simulations have revealed the existence of an azimuthal ExB electron drift instability (EDI) responsible for an enhanced electron cross-field transport (see Sect. 3.4). Lafleur et al. (2016b and 2017) have derived an effective collision frequency to account for the consequence of ExB EDI on cross-field transport. The effective collision frequency associated to each of the phenomena is listed in Tab. II.

Mechanisms	$\boldsymbol{\nu_{e,\mathrm{ano}}}$	**References**
Near-wall conductivity NWC	$\beta_{\mathrm{w}} c_s$	Barral et al. (2003)
Bohm-like	$k_{\mathrm{ano}}\omega_e$	Fife (1998)
Turbulence-shear flow	$k_{\mathrm{ano}}\omega_e \dfrac{1}{1+(A\nabla \mathrm{v}_{de})^B}$	Scharfe et al. (2008)
Turbulence-small scales	$k_{\mathrm{ano}}\omega_e \left(\dfrac{\mathrm{v}_{de}}{c_s}\right)^2$	Cappelli et al. (2015)
Turbulence-wave trapping	$k_{\mathrm{ano}} \dfrac{\lvert\nabla.(\mathbf{u}_i n_e T_e)\rvert}{m c_s n_e \mathrm{v}_{de}}$	Lafleur et al. (2016b, 2017)

Tab. II Functional forms of five anomalous collision frequencies proposed as origins of enhanced electron transport in HT from first-principles analysis. In these expressions, $\nu_{\mathrm{e,ano}}$, A and B are space fitting parameters (constant in time), β_{w} is a coefficient depending on space and time through SEE yield [see Eq. (28)], m is the electron mass, c_s is the ion sound speed, and v_{de} is the azimuthal electron drift velocity [from Jorns (2018)].

In Tab. II, k_{ano} coefficients have been fitted to match measured and calculated integrated over the volume thruster properties such as discharge current and performance (for Bohm transport $k_{\mathrm{ano}} \sim 10^{-2}$, e.g. Hagelaar et al. 2002; Ahedo et al. 2003; and Koo and Boyd 2004). Also, Ahedo et al. (2003) have shown that NWC is not sufficient to explain alone the anomalous transport. Nevertheless, detailed comparisons about local plasma properties (electron density and temperature, ion velocity) have shown the limitation of the proposed approach, even when anomalous transport

is modeled via a combination of phenomena (Barral et al. 2003; Koo and Boyd 2004; Garrigues et al. 2009).

Ongoing research is related to the resolution of a one-dimensional conservation energy equation of the wave energy density (Stix 1962) to self-consistently calculate the anomalous collision frequency in the context fluid/hybrid-based models (Mikellides et al. 2016; Reza et al. 2017; Lafleur et al. 2018). One input of the wave equation is the spatial and time varying instability growth rates (that can be limited to the fastest growing mode responsible for the highest instability amplitude). From linear kinetic theory, dispersion relations are solved to determine the wave angular frequency and growth rate needed for the wave equation. The critical point relies on the choice of energy distribution function that affects the estimation of growth rate. Distributions which are not Maxwellian can be taken from PIC simulations or self-consistently calculated from a particle-test procedure (Monte Carlo or simplified Boltzmann solver in which electric field is taken from fluid/hybrid-based approaches).

The second approach takes the advantage of measurements of local electron and ion properties, and electric potential in the downstream region of the channel and near-field plume. Laser-induced-fluorescence (LIF) technique offers the opportunities to measure the ion energy distribution functions (Dorval et al. 2002; Hargus and Charles 2008; Spektor et al. 2010; Mazouffre 2013). From distribution measurements, moments of Boltzmann equation can be computed to determine the electric field profile (Pérez-Luna et al. 2009; Spektor 2010) and an anomalous electron collision frequency adjusted to match experiments (Ortega et al. 2019; Garrigues et al. 2009). Measurements of electron temperature and density, and electric potential in one or two dimensions in space have also permitted to fit an anomalous electron collision frequency profile (Mikellides et al. 2016; Conversano et al. 2017b). Interestingly, Jorns (2018) has using a genetic algorithm to propose a regressing of the data set coming from intensive measurement campaigns and compare results with attempted theories presented in Tab. II. He has found that the best fit (even if the physical meaning is still unclear) corresponds to $\nu_{e,\mathrm{ano}} \propto \omega_e \left(\frac{c_{si}}{\mathrm{v}_{de}}\right)^2$. From Tab. II, this relation corresponds to a Bohm transport in which the constant k_{ano} depends on space through ratio between sound speed and electron azimuthal drift velocity.

2.5 Nominal operation of the Hall thruster

Fig. 4 illustrates the thruster operation properties for nominal conditions (mass flow of 5 mg/s and applied voltage of 300 V) calculated with the two-dimensional (axial-radial) hybrid model. Empirical parameters were used to fix the anomalous electron transport and energy losses at the walls (see Hagelaar et al. 2002 for details). Results are averaged over 3 ms to eliminate any transient phenomena.

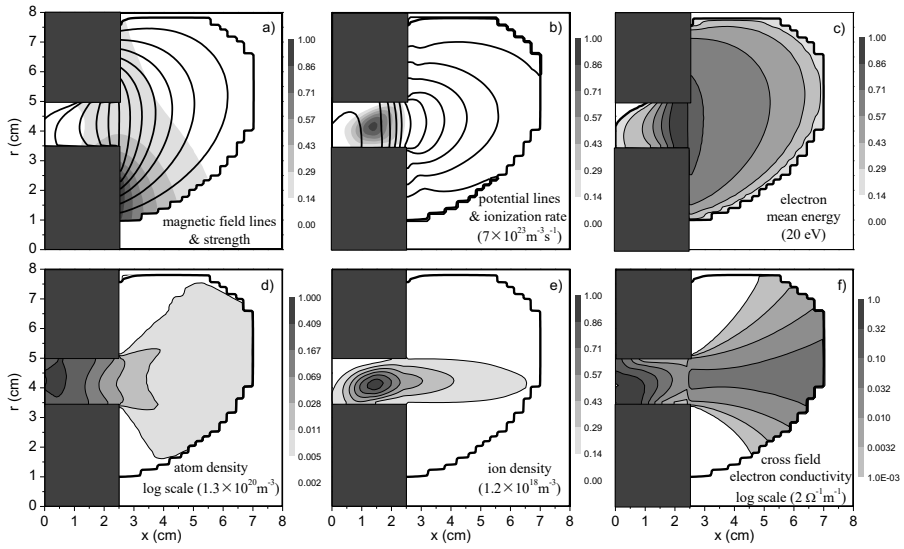

Fig. 4 Time-averaged results for the nominal thruster operation, (a) magnetic field lines and magnetic field strength, (b) electric potential lines (10 contours of 30 V equally spaced) and ionization source term, (c) electron mean energy, (d) atom density, (e) ion density, and (f) electron cross field conductivity. The applied voltage is 300 V and the mass flow of xenon is 5 mg/s. Here x represent the axial coordinate. (Bareilles et al. 2003).

The combination of the 4 external and one internal coils associated with a specific magnetic circuit leads to achieve a predominantly radial magnetic field whose maximum takes place in the vicinity of the exhaust. The shape of the magnetic field forms a convex lens (Fig. 4a). We can distinguish three zones with very different properties. The acceleration region characterized by a large potential drop occurs between x ~ 1.5 cm (here the axial coordinate is represent with x) and the end of the near field plume where a strong magnetic field and low electron conductivity take place. Typically 50 % of the potential drop occurs outside the channel. (The fact that a large fraction of electric potential drop takes place outside the channel is a general trend of HTs in its standard configuration (see e.g. Haas and Gallimore 2001; Linnell and Gallimore 2006; Mazouffre 2013)). It is instructive to compare the shape of electric potential and magnetic field lines. In the near field plume, where the plasma density drops due to ion acceleration and the electron mean energy is moderate, the electric potential field lines are aligned with the magnetic field lines. At the contrary, inside the channel, due to a high plasma density and electron mean energy (~ 20 eV), a non-null radial potential drops occurs and the electric potential field lines now form a concave lens. This comes from the term proportional to electron mean energy and logarithm of plasma density [see Eq.(25)]. The ionization region localized in the center of the channel is characterized by a maximum of ionization source term on the order of 10^{24} m^{-3} s^{-1}. In the same region, the plasma density reaches its maximum (~10^{18} m^{-3}) and the neutral density drops by one order of magnitude. Notice that a shift exists between the maximum of electron mean energy (at the thruster exhaust) and ionization source term. The relative position and overlap of ionization and acceleration regions are mainly influenced by the assumption on the shape of electron-wall losses in the energy equation and on the formulation of anomalous transport in the electron momentum equation. Since the ionization occurs deeply in the channel and upstream of the acceleration region, a fraction of ions generated on the periphery of the ionization source term impacts on channel walls leading to erode them (see Sect. 2.7). The last zone between the ionization region and the anode plane is characterized by a small (but negative) electric potential drop, electrons reaching the anode by diffusion. This region where the magnetic field strength is low and electron transport is essentially controlled by electron-atom collisions is the conduction zone.

The hypothesis made and models used to account for the anomalous electron transport (Sect. 2.4) and electron energy losses on walls do not modify in deep the behavior described above but can almost qualitatively have consequences on the thruster operation and lifetime issues. In Fig. 5, two

sets of simulations have been performed, hybrid #1 with fitting parameters fixed from measurements of discharge current and performance (dashed lines), and hybrid #2 where the electron cross-field mobility profile is adjusted to fit measured ion velocity profiles (full lines). The length of the acceleration region is overestimated in the case of description of anomalous transport with fitting parameters, and consequently the maximum of electric field is underestimated. Shortening the acceleration region by adjusting the mobility profile also modifies the energy gained by the electron at the channel entrance that has consequences on the ionization region. In hybrid # 2, the ionization of neutral atoms occurs less deeply in the channel. This result highlights the necessity to proper account for the electron anomalous transport in hybrid/fluid models of HTs.

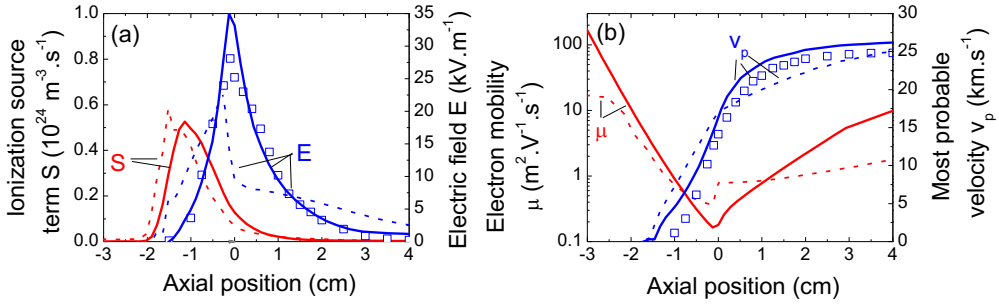

Fig. 5 Time-averaged profiles along the PPS®X000-ML thruster channel centerline, (a) ionization source term and computed and measured (square symbols) electric field profiles, (b) electron cross-field mobility and computed and measured (square symbols) ion velocity profiles. The applied voltage is 500 V and the mass flow of xenon is 6 mg/s (Garrigues et al. 2009).

2.6 Operating regimes and wall effects

In the context of HTs, a classification of operating regimes has been overviewed by Zhurin et al. (1999) and Choueiri (2001). Most of the works presented in the two reviewed papers were based on former Soviet Union's studies of the 1970s with an old design, where the position of maximum of magnetic field was located inside the channel. At fixed xenon mass flow, discharge current was measured as a function of discharge voltage (respectively magnetic field) for a given magnetic field (respectively discharge voltage). Correlated to discharge current, measurements of the spectrum (amplitude and frequency) and plasma properties through Langmuir probes has permit to classify the thruster operation in different categories.

In the last 15 years, a large effort to characterize and understand the influence of the type of wall materials on "modern" HT operation and performance has then been undertaken. The main goal was to revisit the different categories and the range of parameters (mass flow, voltage, magnetic field, and wall materials) for which the thruster can operate in its nominal mode with high performance. The nominal mode can be characterized by a high ionization of the neutral gas, a maximum ratio between ion and discharge currents to maintain a low electric power, and a minimum of the amplitude of current oscillations (necessary for the architecture of power processing unit and cathode operation). Mode transitions have been established through experimental campaigns for variable discharge voltages and magnetic field strengths for a SPT-100 together with calculations (Gascon et al. 2003; Barral et al. 2003; Hara et al. 2015) and for variable magnetic field strengths for the 6kW H6 (Sekarak et al. 2016). New studies have been reinforced by the implementation of time-resolved diagnostics including CCD fast camera and optical fibers (e.g. Bouchoule et al. 2001, Ellison et al. 2012; Sekarak et al. 2016; Mazouffre et al. 2017) that are capable to offer a new insight of the plasma dynamic in the 5-30 kHz range.

In this section, we illustrate the different operating regimes through measured and calculated current characteristics for variable discharge voltages and we focus on one specific regime so-called breathing mode observable in HTs.

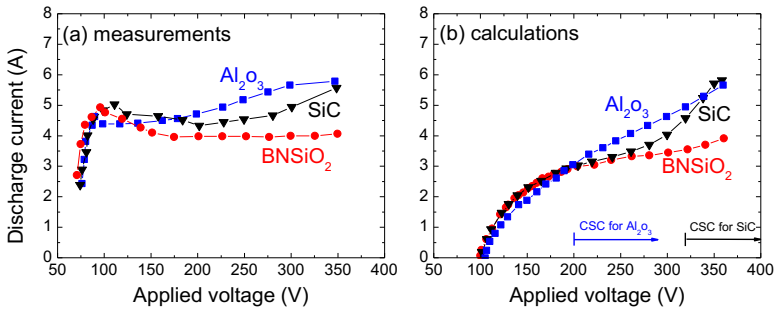

Fig. 6 (a) Experimental and (b) calculated dc current-voltage characteristics for three different wall materials for a SPT-100. The mass flow of xenon is 5 mg/s and the magnetic field is kept the same (Gascon et al. 2003 and Barral et al. 2003).

Fig. 6 reports comparisons between measured and calculated (with a one-dimensional axial fluid model) I-V curve. Before a threshold voltage of few tens of volts, the discharge is impossible to ignite and/or not stable. Depending of the type of materials, two or three different regimes can be distinguished. A first regime below corresponds to a sharp (larger in experiments) increase of the current. In that zone of low discharge voltage, and low electron mean energy associated, the neutral atoms are not completely ionized. The high (almost in experiments) current discharge is carried by the electrons. The measured discharge current exhibits time fluctuations whose amplitude corresponds to 10-50 % of the dc discharge current at a frequency of 5-10 kHz. For $BNSiO_2$ material, high-speed imaging shows that a stable rotating structure in the $E\times B$ (azimuthal) direction appears at large wavelength (mode m = 1) (Sekarak et al. 2015; Mazouffre et al. 2017). Such structure cannot obviously being captured by axial one-dimensional or axial-radial two-dimensional models. Only axial-azimuthal hybrid simulations of Lam et al. (2015) at 100 V predict a 40 kHz instability of mode m = 1, 2 rotating in the azimuthal direction in the quasi entire channel at a low velocity phase (~ few km/s).

The second regime corresponds to a constant discharge current variation (quasi-constant in calculations) that happens during a wide range of discharge voltages for $BNSiO_2$, on a limited range of voltages for SiC and is quasi-absent for Al_2O_3. For $BNSiO_2$, electrons are sufficiently heated to largely ionize almost all the neutral atoms injected and the ion current contributes to ~ 0.8 of the discharge current. The amplitude of the fluctuations of the discharge current varies from 10 to 20% of the dc current with a frequency of ~ 20 kHz. This region corresponds to the nominal operation of the thruster. In a third regime, visible in Fig. 6 for alumina and silicon carbide materials (but also observed at discharge voltages larger than 500 V for $BNSiO_2$), the frequency is almost the same but amplitude of current oscillations can exceed 100% of the dc current obtaining a pulsed discharge regime. The studies have confirmed that $BNSiO_2$ is the best candidate for a HT to operate efficiently in the expected range of performance.

Barral et al. (2003) have attributed the transition between the two regimes to the SEE effect on sheath properties. As the electron mean energy increases and reaches the first crossover energy E^* (see Appendix 1 for details) and $\bar{\sigma} \rightarrow \bar{\sigma}_{SCS}$, the sheath becomes space charge saturated and the contribution of electron-wall interactions on cross-field transport and energy losses play a major role on the discharge properties. The order of appearance of this regime found in simulations is consistent with the first crossover energy E^* of materials (early with Al_2O_3 and very far for $BNSiO_2$). No fundamental differences have been obtained with two-dimensional fluid/hybrid models. Calculations only including SEE as anomalous process able to enhance the electron cross-field transport also underestimate the discharge current. No systematic study of discharge current variations on a wide range of voltages (or magnetic field) has been performed when the electron anomalous transport is determined by adjusting the cross-field mobility profile to match experimental and calculated ion velocity profiles.

The regime of discharge current oscillating at 20 kHz called breathing mode has extensively been characterized and studied in the literature. The breathing mode is visible in Fig. 7 through measurements of the plasma emission by means of high-speed image recording (period of 30 μs) and calculations of plasma properties with the hybrid axial one-dimensional model (Boeuf and Garrigues 1998). The so-called breathing mode is associated to a periodic depletion of neutrals in the region of high magnetic field and high electron temperature leading to an increase of plasma density and discharge current (through the ion component). A certain delay in time is needed for neutral atoms to again fulfill the ionization region. During this time, the ionization drops and plasma density and discharge current decrease. The frequency of these oscillations is roughly inversely proportional to the time needed for the neutrals to fulfill the ionization region related to the large magnetic region near the exhaust. This is qualitatively confirmed by measurements of plasma emission in channel exhaust showing alternate phases of high and very low plasma emission. Results have been also confirmed by spectroscopic measurements studies (Touzeau et al. 2001).

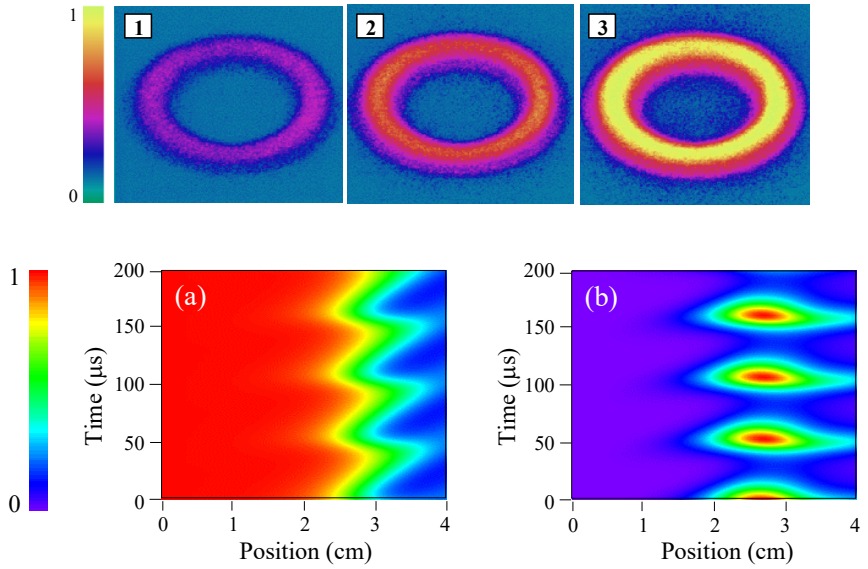

Fig. 7 (top) Emission of the plasma during one cycle of oscillation, (bottom) calculated plasma properties (a) neutral density (maximum of 1.6×10^{19} m^{-3}), (b) plasma density (maximum of 1.6×10^{18} m^{-3}). The anode is at z=0 cm and the exhaust at z=4 cm. The HT is a SPT-100 with $BNSiO_2$ wall materials. The mass flow of xenon is 5 mg/s and the discharge voltage is 280 V (Darnon et al. 1999).

2.7 Erosion model and calculation of thruster lifetime

One critical issue of Hall thruster is the wall erosion since with the existence of a radial electric field inside the channel, ions generate downstream interact with walls (see Sect. 2.5 and Appendix 2 for ion sputtering models). Using fluid/hybrid two-dimensional models of Hall thruster, since 10 years ago, intensive studies have been performed to estimate wall erosion and thruster lifetime. The end of thruster lifetime is characterized by the erosion of the ceramic wall thickness at the channel exhaust where the flux and energy of ions are the strongest. When it occurs, the magnetic circuit and coils are now directly exposed to the plasma. The power deposition further induces a large modification of the optimum magnetic field topology that degrades the thruster performance in its nominal operation. To predict the thruster lifetime, the strategy adopted is the following. The channel walls are decomposed in sub-segments (whose length corresponds at the minimum to one computational cell size) in which the eroded thickness is calculated. When a steady state regime is achieved and for an appropriate time fixed (equivalent to typically 100 hours, corresponding to successive channel wall erosion measurements during long-life testing), the channel geometry and magnetic topology are changed and new plasma and erosion properties can be again computed

accordingly. The process is repeated until the simulation of 1000-5000 hours of thruster operation. Deformation of grid cells inside the eroded zone of the computational domain has also been considered (e.g. Koizumi et al. 2008).

In Fig. 8, the history of erosion of inner and outer walls of the Stanford HT gives a representative vision of how erosion affects the channel wall profiles for a 1 kW-class HT (Sommier et al. 2005). Typically half of the erosion occurs in the first 1000 hours of life. Aa asymmetry in the erosion is also visible Fig. 8, certainly caused by the magnetic topology and non-uniform plasma properties in the radial direction. The origin of the erosion drop is attributed to the angular dependence of sputtering yield which is maximized for an angle of 70 degrees relative to normal incidence (see Appendix 2). Most of ions contribute to erode the surfaces. During the thruster life, the increase of the surface tilt angle has obviously a benefit effect on the reduction of erosion process (Yu and Li 2007). In the literature, during thruster life, a time continuous decrease of the thruster performance has been observed, attributed to a decrease of potential drop inside the channel (Yim et al. 2006) and by a decrease of plasma density (Sommier et al. 2005).

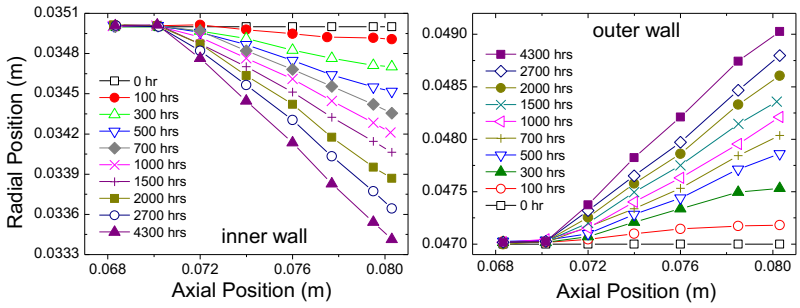

Fig. 8 Simulation of channel wall erosion of the Stanford Hall thruster (from Sommier et al. 2005).

Cheng and Martinez Sanchez (2007) have simulated the operation of the 200 W Busek HT, the BHT-200. Simulated channel wall profiles for 500 hours of operation compare well with experiments, predicting of lifetime of ~ 1300 hours. They have also simulated the BHT-600 and explained higher wall erosion by the presence of doubly charged ions. They highlight the fact that tuning the anomalous coefficients for cross-field transport to successfully capture the erosion profile is not a guarantee that others calculated parameters (discharge current and performance) correspond to experiments (and vice versa). The question of time evolution of anomalous coefficients during the changes of channel geometry is also opened.

2.8 Magnetic shielded configurations

The strong influence of wall materials on thruster lifetime (through erosion mechanism) and performance (through SEE processes) is an established fact. This is especially true for small size HTs where plasma-wall interactions play a major role. One can imagine pushing the ionization and acceleration regions outside the channel. The so-called wall-less HT is based on this principle. The channel geometry corresponds to the standard one, except that the maximum of magnetic field occurs in the near-field region and the anode position is shifted close to the exhaust. If preliminary results show a decrease of performance, the wall-less configuration takes advantage of keeping a simple magnetic field configuration and the channel length that can be shortened (Mazouffre 2016).

In this section, we focus on the proposition of a new magnetic field configuration able to prevent or almost reduce plasma-wall interactions. In the standard magnetic field configuration shown in Sect. 2.5, wall erosion is caused by a non-null radial electric field component that leads to ions generated at the edge of the channel to interact with walls. This is further amplified by a high sheath potential drop induced by a high electron temperature in the acceleration region (see Fig. 8 on the left). An

original magnetic field topology called shielded configuration has been proposed. Its consequences on electron temperature and electric potential lines are illustrated in Fig. 9 on the right. The main idea is to keep a cold electron temperature (as close as possible to the anode one) inside the channel. In this manner, the radial electric field diminishes [see Eq. (25)], the sheath potential drop remains low [eq. (27)] and plasma-wall interactions are consequently strongly reduced. Of course, the magnetic field configuration proposed by Morozov's with a convex shape of magnetic field lines together with a maximum of magnetic field strength localized in the exhaust cannot be achieved. As far as the electric and magnetic fields are perpendicular, the electrons trapped by a radial magnetic field and heated in the acceleration region are intercepted by the walls at high energy. The adopted solution is to force the magnetic field lines to be almost parallel to the walls in the downstream section of the channel. Due to cold electrons coming from the anode, the magnetic field lines tangent to the walls make possible maintaining a low energy close to the walls. Thanks to a chamfering surface, magnetic field lines are not intercepted by the channel walls in the vicinity of the exhaust.

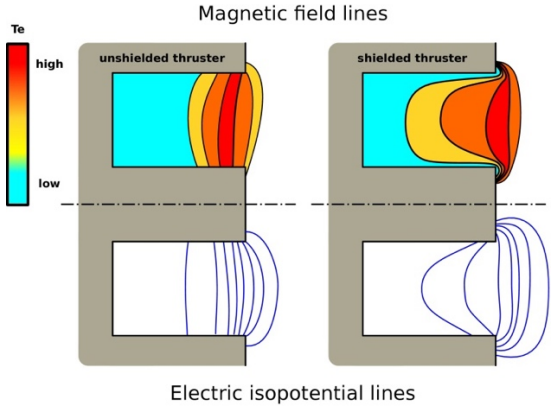

Fig. 9 Comparison between standard and magnetically shielded HT configurations (Garrigues et al. 2018).

The Jet Propulsion Laboratory from NASA has designed, built and successfully tested magnetically shielded HTs in the range of high (e.g. 9 kW-class H9 described in Hofer et al. 2017) and low (200-W class MasMi Hall thruster, Conversano et al. 2017a, 2017b) powers through combination and intense go back between experiments and numerical simulations with a two-dimensional axial-radial fluid model (e.g. Mikellides et al. 2013, 2014a, 2014b). Comparisons of measured and simulated electron temperature and electric potential profiles are shown in Fig. 10 with the original magnetic field labeled unshielded (US) and the new magnetically shielded (MS) configurations. Results of Fig. 10 qualitatively validate the desired effect of MS configuration. Despite discrepancies between experiments and calculations, an almost flat electric potential profile (very close to discharge potential) is achieved in the MS configuration while a large potential drop occurs in the US configuration. As a result, the electron temperature close to the walls is lowered in the MS configuration with a quasi-flat profile. Calculations of wall properties have revealed a decrease of erosion by 3 orders of magnitude, the quasi-absence of erosion in the MS configuration has been later experimentally confirmed (Mikellides et al. 2014b). Results show that wall erosion can be effectively eliminated as a practical consideration in HTs. Importantly, calculations also show that the ionization region is concentrated in the exhaust plane, and the acceleration region mostly occurs in the near field plume (e.g. Grimaud and Mazouffre 2017a; Garrigues et al. 2018), that are in part also responsible for a lowering of the erosion of the channel walls. Finally, Grimaud and Mazouffre (2017a) have also shown that replacing $BNSiO_2$ by a conducting material (graphite) does not drastically change the thruster performance offering interesting perspectives in term of thruster operations.

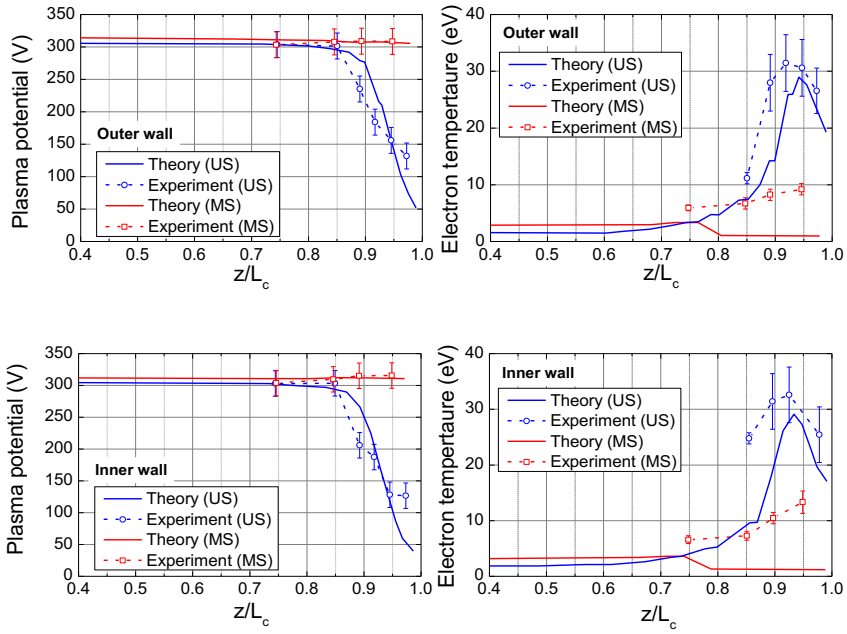

Fig. 10 Comparisons between numerical simulations and data from wall probes for the 6 kW-class H6 HT of electron temperature and plasma potential profiles. The channel exhaust is at $z/L_c = 1$. The discharge voltage and current are 300 V and 20 A, respectively (from Mikellides et al. 2014a).

3 Full kinetic models

Due to the weak collisional nature of electrons in HT (electron mean free path is hundreds times larger than device dimensions) the electron distribution function is expected to be different from the Maxwellian behavior. Guerrini et al. (1997) and Morozov-Savelyev (2000b) already predicted the presence of three groups of electrons in the thruster channel: (1) low-energy electrons with energy of the order of several eV; (2) middle energy tail reaching up to 20–30 eV; (3) high-energy peak in the electron energy distribution function (EEDF), observed near the anode. The group of low-energy electrons consists of those prevented from striking the walls by the radial electric field (so called "trapped" electrons: they rotate as a solid body and their velocity distribution function is well described by a linear spline (Bugrova et al. 1992). The electrons that elastically collide with the walls (backscattered) belong to the "escaping" high-energy group. Clearly, their energy increases close to the anode. Finally, the "intermediate" group is formed by electrons with energy sufficient to reach the walls and undergoing inelastic collisions there. Correspondingly, the intermediate particle energy lies between the maximum energy of the trapped particles and the minimum energy of the escaping electrons. The total distribution varies with the location in the channel (see Fig. 11). In the electron generation zone (ionization and exit plane regions) only "trapped" electrons exist. The three groups of EEDF begins to be more evident as it goes from the generation zones towards the anode.

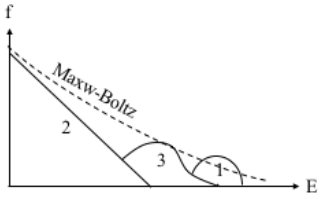

Fig. 11 The general shape of an EEDF in HT: 1) "escaping", 2) "trapped" and 3) "intermediate" electrons. For comparison the equilibrium Maxwell-Boltzmann distribution is reported with dashed line.

The deviation from Maxwellian behavior is further increased due to additional mechanisms, such as the presence of anisotropy due to the magnetic field (the electron temperature in the direction parallel to B can be $T_{e,\parallel} \approx 10$ eV, several times smaller than the electron temperature perpendicular, $T_{e,\perp} \approx 40$ eV) and the interaction with the walls (loss cone and beam-like secondary electrons).

The non-Maxwellian character has at the end macroscopic effects on global phenomena such as instability, wall losses and sheath, ionization rate, electron cross field mobility, etc. Controlling of electron transport and plasma-wall interaction could lead to a technologically superior thruster with larger efficiency. It is therefore necessary to describe the kinetic nature of the electron subsystem solving for the corresponding Boltzmann Eq. (1).

In this regard, two different kinetic approaches can be found in literature, one using direct solvers of the Boltzmann Eq. (1) and the other using the well know Particle-in-Cell / Monte Carlo Collision (PIC-MCC) methodology (Hockney-Eastwood 1989 and Birdsall-Langdon 2005). The typical PIC-MCC scheme has been presented in Sect 2.1 for ions. In fully kinetic PIC models of HTs (Taccogna et al. 2007, 2008a), the same operations done for ions are also processed for electrons and the collisional module is tackled by the Monte Carlo Collision approach (Taccogna 2015). Knowing the charge density on the mesh nodes, the self-consistent electric field is calculated by solving the Poisson equation. In the explicit version, a PIC-MCC model requires important constraints: 1) cell-size Δx smaller than the Debye length; 2) timestep Δt smaller than the inverse of the plasma frequency; 3) particles not moving more than one cell during the timestep; 4) number of particles per cell larger than 50-100. With the typical HT plasma parameters, these give $\Delta x < 30$ μm and $\Delta t < 5 \times 10^{-12}$ s.

3.1 Boltzmann solver models and electron energy distribution function (EEDF)

Different studies have made use of the direct Boltzmann solver for electron distribution function. All heavily use approximations or fixed experimental values for some quantities in order to make the Boltzmann Eq. (1) mathematically manageable. Expressions for the EEDF have been derived in Fedotov et al. (1999), Shagayda (2012) and Shagayda and Tarasov (2017) neglecting the electron-wall collision. The first have interpreted the EEDF as a beam-plasma electron distribution function with electron beam energy of several tens of eV. The contribution of the electron beam was shown to be essential in the ionization of the working gas. The latter two works have obtained an analytical solution of the electron kinetic equation in a homogeneous and non-homogeneous (density and temperature gradient effects) plasma. In the limit of large Hall parameter, the solution comes down to the product of the Maxwell function into a combination of modified Bessel functions of the first kind (Fig. 12). This kinetic corrections leads to significant rate of diffusion across the magnetic field when the drift velocity $v_{d,e}$ in the ExB direction is comparable with the thermal velocity of the electrons $v_{th,e}$.

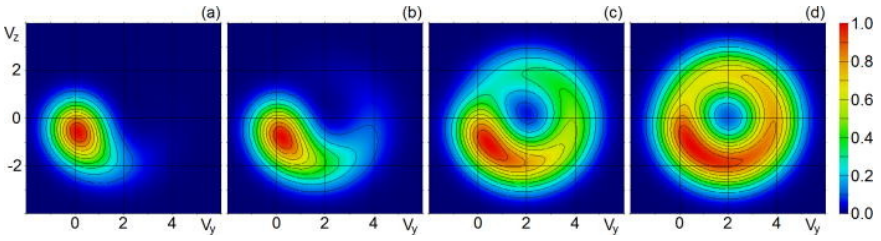

Fig. 12 Electron velocity distribution function in uniform plasma for $v_{e,d}/v_{e,th}=2$ and for four different Hall parameters $\Omega_e=0.5$, 1, 3.3 and 10. Here v_y represent the azimuthal component. The figure is taken from Shagayda and Tarasov (2017).

Numerical solvers of the electron Boltzmann equation including the electron-wall collision with secondary electrons from the wall were implemented by Latocha et al. (2002) using a Hilbert expansion method and by Meezan-Cappelli (2002) using a two-term Lorentz approximation. The SEE yield and the emitted electron energy spectrum used were simplified (see Appendix 1). Both models shows that the EEDF is depleted at high energy due to electron loss to the walls and that electron wall-loss and wall-return frequencies are extremely low compared to those predicted by a Maxwellian of equal average energy. The very low frequency of wall collisions suggests that the space charge-saturation (SCS) limit does not appear and that NWC do not much contribute to the total cross-field transport.

All previous Boltzmann solver models do not solve Poisson equation for the self-consistent field but they use local field limit, using the experimental results as inputs. The first numerical solution of the self-consistent Vlasov-Poisson system for electrons appeared with Morozov-Savelyev works (2002, 2004 and 2007) where the Debye layer is studied taking into account SEE. For the first time, an oscillatory quasi-periodic sheath behavior (sheath instability) and inverse Debye layer regimes have been observed beyond the SCS for high electron temperature.

3.2 PIC Radial models: lateral sheaths, secondary electron emission and near-wall conductivity

Particle models are suitable for simulating the non-neutral region attached to the dielectric walls in HT. They allows to solve self-consistently the Poisson equation (see Appendix 3 for the different software packages available) and to faithfully reproduce the complex phenomenon of SEE. As a consequence, a more quantitative assessment of the effect of NWC on the electron anomalous transport can be done since this mechanism strongly depends on the characteristic of the Debye layer and on the non-Maxwellian character of the electron distribution function.

The dielectric nature of the walls implies that the potential must remain floating guarantying a net zero current collected at the wall $I_w(t)=0$. Generally, three way are developed to account for this:

(a) using a capacitor-like equation

$$C\frac{d\phi_w}{dt} = I_w, \quad (31)$$

where the numerical parameter C can be interpreted as a surface capacitance and its value is chosen as a trade-off between low statistical noise and small response delay. Eq. (31) adjusts ϕ_w to counter the net charge accumulated at the wall;

(b) solving for the general Poisson equation including the dielectric material and moving the boundary conditions at the end of the dielectrics: one extreme coincides with the axis of symmetry and therefore requires that

$$\frac{d\phi_0}{dr} = 0 \quad (32.a)$$

while the other extreme represents the reference potential (Dirichelet condition)

$$\phi_{Nr} = \phi_{ref}; \quad (32.b)$$

(c) solving Poisson equation using Neumann boundary conditions on both the plasma-wall interfaces assuming the electric field inside the material as negligible:

$$\frac{d\phi_w}{dr} = \pm \frac{\sigma_w}{\epsilon_0} \quad (33)$$

where σ_w is the surface charge density accumulated at the current PIC cycle. The ± sign referees to the outer and inner wall, respectively, if the reference system is set such that the inner wall represent the first mesh node and the outer wall the latest.

The first PIC-MCC model of the electron radial dynamics in HT can be traced back to the work of Jolivet and Roussel (2000) who highlighted the importance of partial thermalization and penetration of secondary electrons leaving one sheath, crossing the channel and entering the opposite sheath. Following this seminal work, Taccogna et al. (2005a, 2006a, 2008b, 2009, 2014a) and Sidorenko et al. (2006, 2007, 2008, 2009) developed an explicit cylindrical and implicit cartesian, respectively, 1D radial-3V PIC-MCC model of the plasma bounded between the channel walls with a sophisticated SEE module (see Appendix 1). The models only require as input parameters, a prescribed initial plasma distribution (density and temperature) and fixed axial electric field (range of 50-200 V/cm), radial magnetic field (about 100-200 Gauss) and neutral density.

Among the many results obtained with these models (the depletion of electrons in the tail of the distribution above the sheath potential, the presence of secondary beam electrons and the anisotropy between radial and axial directions are evident in Fig. 13), we can mention:

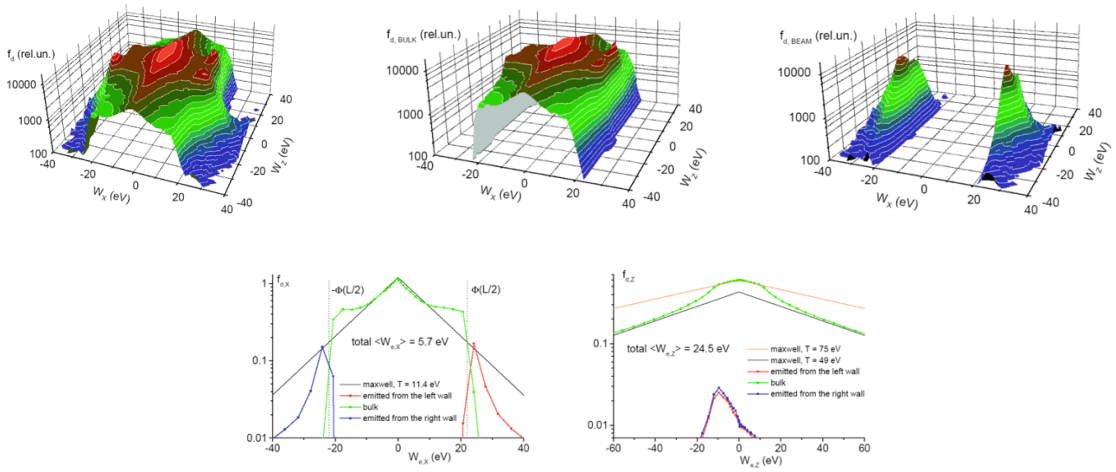

Fig. 13 Electron velocity distribution function (EVDF) projected on the radial (here indicated with x) and axial z components, decomposed in bulk primary and secondary electron components on the top. On the bottom the projection along the radial and the axial directions are reported showing the marked anisotropy $T_{ex} \ll T_{ez}$. The vertical dashed lines represent the potential in the middle of the channel between the two walls. The SEE beams distributions are non-symmetric due to the cyclotron rotation. Courtesy from D. Sydorenko.

- the importance of secondary electron beam limiting the maximum electron temperature and producing most of the electron current to the walls with possible sheath and two-stream instabilities;

- significant asymmetries at the inner and outer walls for the collected currents, the mean impact energy, and the sheath potentials, due to the combination of the geometric expansion (cylindrical geometry), the magnetic mirror effect, and the centrifugal force (emanating from the E × B drift);

- the departures from the Boltzmann relation along the magnetic lines due to temperature anisotropy and non-uniformity, and to the centrifugal force;

- the detection of a new regime of plasma-wall interaction where the plasma-sheath system performs relaxation oscillations by switching quasi-periodically between the SCS and non-SCS states (see Fig. 14). The oscillation cycle starts when the sheath enters the SCS regime. Once a wall encounters an intense flux of cold electrons from the opposite wall, the SCS regime quenches, the high plasma potential restores, and a large number of cold secondary electrons become trapped inside the plasma. Then, these electrons are heated until the sheath becomes unstable again.

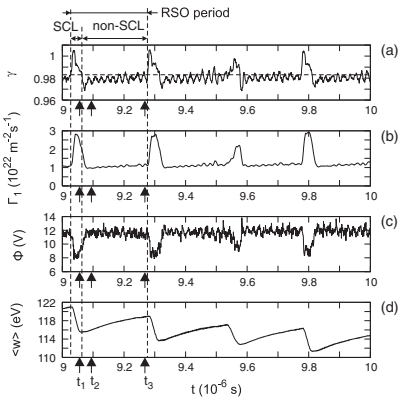

Fig. 14 Temporal evolution of (a) SEE yield, (b) primary electron flux, (c) plasma potential and (d) averaged electron energy at the wall. Dashed vertical lines mark the beginning and the end of the relaxation sheath oscillation (RSO) period and the transition from SCS to non-SCS state. Dashed horizontal line in (a) marks a theoretical value of the critical emission coefficient γ_{SCS}=0.983 for a Xe plasma with a Maxwellian distribution. The figure is taken from Sidorenko et al. (2009).

Accounting for the depleted loss cone of the velocity space in the direction perpendicular to the wall, Kaganovich et al. (2007) provided analytical estimates of the wall potential, electron-wall collision frequencies, and energy loss frequency showing that the fluid approach leads to large overestimations of these quantities.

Further developments of Taccogna and Sidorenko models have been carried out by Domínguez-Vázquez et al. (2018a), and Campanell et al. (2012a, 2012b, 2012c, 2013, 2015), Wang et al. (2014), respectively. The first have implemented more sophisticated algorithms to adjust the mean neutral density to the desired mean plasma density, to avoid the refreshing of axially accelerated particles by ignoring the effect of E_z on updating the axial velocity and to correctly weigh low-density secondary electron populations. The second recover regimes of sheath instability and inverse sheath when the SEE yield induced by secondary beam electrons emitted from the other wall exceeds 1. Furthermore, they have shown the importance of secondaries energy spectrum and the amplification mechanism due to back-reflection of secondary electrons.

A two-dimensional extension of the radial sheath model has been implemented by F. Zhang et al. (2011, 2014) to detect spatial modulation of the sheath along the axial dimension for very large secondary electron emission. Another two-dimensional sheath model studying the effect of emissive grooved surfaces (mimicking the effect of the ion erosion on the lateral walls) have been done by Schweigert et al. (2018).

Finally, deserving of mention are also particular kinetic approaches used in the works of Ahedo-De Pablo (2007) and Miedzik et al. (2015) who have used semi-analytical approaches and quasi-neutral PIC with guiding center approximation, respectively, to solve the plasma-surface transition region in HT. The first work takes into account the combined effects of partial depletion of the main electron population and partial recollection of the SEE beams by using a partial thermalization parameter. Simple expressions for sheath, particle and energy losses were derived. The approximations done into the model were valid for magnetic lines perpendicular to the wall and

weak enough axial (parallel to the wall) electric field E_z. On the contrary, the second work aimed to study the effect of inclination of the magnetic field with respect to the channel walls. It has been shown that oblique magnetic field significantly impacts the electron temperature anisotropy, the plasma sheath parameters, and the SEE yield. To a lesser extent, the cross-field electron drift is also affected, but the modification was found only significant for field lines near grazing incidence with the walls.

3.3 PIC axisymmetric models: Axial acceleration mechanism and ion erosion

Different 2D(r,z) axisymmetric models (Taccogna et al. 2004a, 2005b, 2006b, Liu et al. 2008, Matyash et al. 2010, Yu et al. 2011, 2012, Kronhaus et al. 2012, Quing et al. 2014, Szabo et al. 2014, Cho et al. 2013, 2015 and Kahnfeld et al. 2018) have been developed to simulate the channel discharge and part of the near-field plume region. Often, numerical tricks, such as smaller ion to electron mass ratio, larger vacuum permittivity and geometrical scaling (Taccogna et al. 2005c), are used to alleviate the high computationally demanding constraints of fully kinetic PIC models in order to accelerate the simulation execution. The obvious problem related to these different scaling schemes is that some important non-dimensional plasma parameters are not conserved with consequences on non-linear phenomena associated with these parameters (e.g., plasma sheath, instability, etc.).

The extension of the radial model to include the axial coordinate allows to self-consistent sustain the discharge by taking into account the source terms due to the axial contribution (electrons from the plume or ionization zone, and ions from the ionization zone). In fact, in all the models that do not include explicitly the axial dimension z, the way to sustain plasma is unavoidably artificial. In these cases the simulation starts with an initial plasma distribution and a global neutrality is garanteed injecting the right number of electrons / ions necessary to keep the total number of macropaticles fixed. This maintains an average constant value of density and roughly models a random flux of particles representing the axial source term. Differently, in the two-dimensional axisymmetric representation, the simulation can start from the scratch and the discharge ignition phase can be reproduced. Taccogna et al. (2006b) and H. Liu et al. (2008) have used their models to describe the start transient phase.

Given the lack of the azimuthal coordinate, anomalous transport induced by the azimuthal fluctuation is modeled through an equivalent collision frequency (see Sect. 2.4) $\nu_{e,ano} = \frac{1}{\beta}\omega_{ce}$ whose only effect is to scatter the electron velocity without adding or subtract energy from electrons. The parameter β (16 is its fully turbulent Bohm limit) is used as axially dependent free parameter to best match experimental quantities (discharge current, anode efficiency and thrust): its value ranges between 50 and 500 (see Fig. 15). Due to the axisymmetric character, this class of simulations captures many physical features of the discharge, including wall effects, breathing mode (when neutral dynamics is included) and ion transit time oscillations and is able to quite reasonably predict global performances (less than 20% in thrust and discharge current) and current-voltage characteristics of HT. Axial profiles of plasma parameters often compare well with experimental measurements. For this reason, these models are used to investigate different variant of HT (cathodic arc as in Lüskow et al. 2018) and in particular alternative magnetic field configurations (the ATON double stage type by Liu et al. 2008 and Yu et al. 2012, CAMILA design by Kronhaus et al. 2012, and HEMPT by Matyash et al. 2010 and Kahnfeld et al. 2018) and the effect of intermediate segmented electrodes (by Yu et al. 2011 and Quing et al. 2014). Axisymmetric models can diagnose the particle and energy flow to the walls as a function of the axial coordinate they can also assess the wall erosion due to ion sputtering (see Sect. 2.7). The effect of the cathode location (often out-of-axis) in the plume cannot be captured.

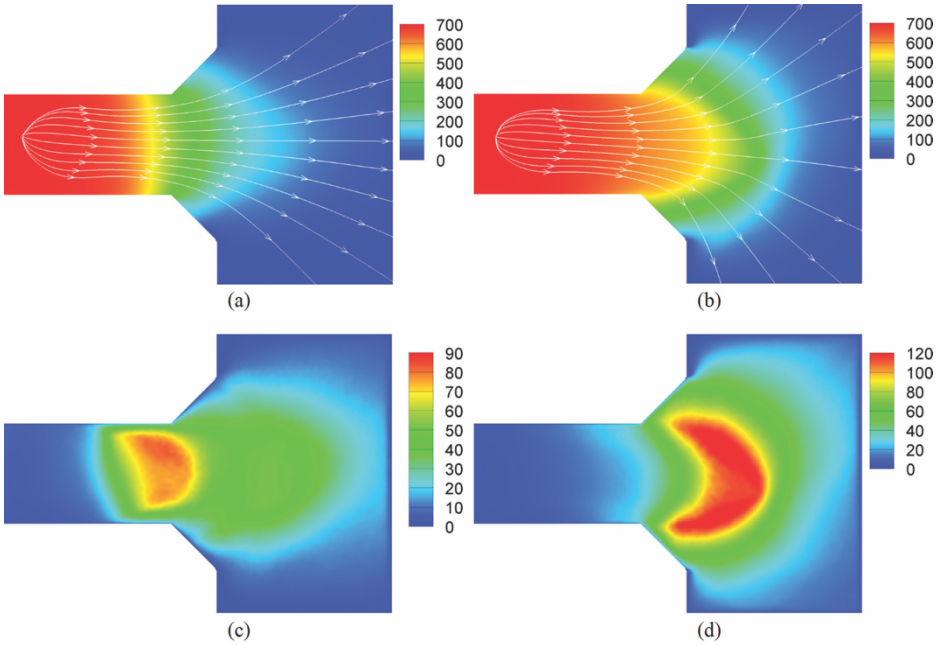

Fig. 15 Effect of the anomalous collision $\nu_{e,ano}$ with β=16 on the plasma potential and mean kinetic electron energy: (a) Plasma potential (V) using anomalous collision $\nu_{e,ano}$ overlaid with ion-stream traces, (b) plasma potential (V) without anomalous collision overlaid with ion-stream traces, (c) mean kinetic energy of electrons (eV) using anomalous collision $\nu_{e,ano}$, and (d) mean kinetic energy of electrons (eV) without anomalous collision. Results come from 2D-axisymmetric PIC model for HT operation condition of 750 V discharge voltage and 2 mg/s Xe mass flow rate (Cho et al. 2015).

3.4 PIC Azimuthal models: the electron cyclotron drift instability

As seen in the previous Sect. 3.3, axisymmetric models use empirical, adjustable cross-field mobility to take into account the anomalous transport induced by azimuthal modulations. It has been proved (Lafleur et al. 2016b and Lafleur 2017) that it can be written in the following form:

$$\mu_{\perp,\theta} = \frac{\mu_0 h}{1+h^2} \frac{<n_e E_\theta>}{n_e E_z}. \quad (34)$$

The brackets <> represents the correlation between the azimuthal modulations of electron density and azimuthal electric field. One of the most likely candidate to drive such a fluctuation is the large Hall current flowing in the azimuthal direction. It is the origin of a microscopic instability, known as ExB electron drift instability (EDI). It results from the shifting of electron Bernstein waves toward low ion acoustic frequencies by the Doppler effect induced by the large ExB electron drift velocity v_{de}. The solution of the corresponding dispersion relation shows that when components along the magnetic field are neglected, wave numbers result to have large resonances at discrete values:

$$k_{\theta,n} = n\frac{\omega_{ce}}{v_{de}} \quad (35)$$

while the frequency is close to the ion plasma frequency $\omega \approx \frac{\omega_{pi}}{\sqrt{3}}$ (at the maximum growth rate). For non-zero k_r, the discrete nature disappears and the solution of the dispersion relation simplifies to a modified ion-acoustic type relation.

This instability has been analyzed in detail by different 1D-azimuthal PIC models (Ducrocq et al. 2006, Boeuf 2014, Lafleur et al. 2016a, Jahnunen et al. 2018a and Katz et al. 2018) assuming fixed axial electric and radial magnetic fields in cartesian geometry and using a periodicity length along

the azimuthal coordinate always smaller than the real one. Steady state solutions are only obtained if particle loss from the virtual axial boundaries is included: particles are still tracked along the axial direction and each electron (resp. ion) leaving the simulation domain on the anode (resp. cathode) side is replaced by a new electron (resp. ion) at the cathode (resp. anode) side. This particle re-injection mechanism, necessary to avoid undesirable secular effect and to mimic the axial transport, works at the end as extra collision in the model.

All these studies have confirmed a significant fluctuation amplitude of ExB drift instability characterized during the linear stage by high-frequency (of the order of MHz) and discrete number of short-wavelengths (of the order of mm) corresponding to the first cyclotron harmonics Eq. (35). An important feature observed is the difference in the ion and electron density fluctuations. While the electron density perturbations are lower amplitude, the ion density perturbations have much larger amplitude and contain much shorter wavelength (non-quasineutral) content with $k_\theta \lambda_{De} \geq 1$.

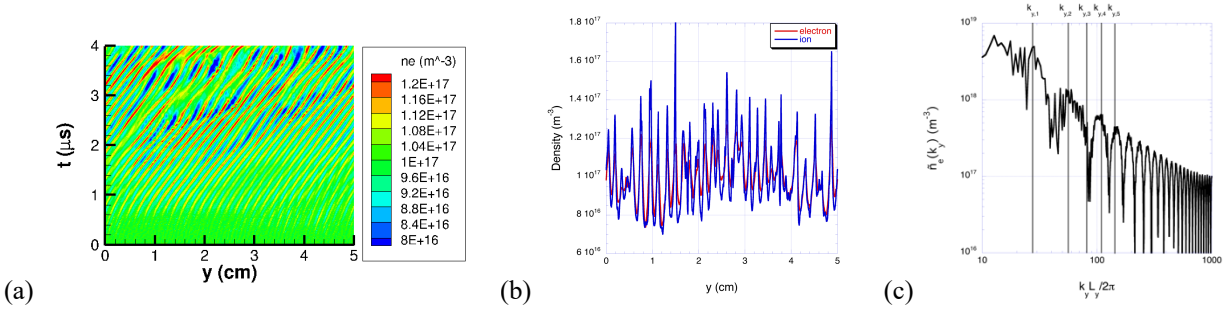

Fig. 16 (a) Temporal evolution of the electron density profile along the azimuthal direction y. (b) Electron and ion density azimuthal profiles at t=4 μs and (c) amplitude of electron density spectral components [the first five cyclotron harmonics Eq. (35) are shown]. Results come from 1D-azimuthal cartesian PIC model using an azimuthal domain of L_y=5 cm and a number of particles per cell of N_{ppc}=2.5x10^4.

The saturation mechanisms of the instability have been identified in the electron heating, deformation of the electron distribution function projected along the azimuthal direction and ion-wave trapping. No consensus have been found instead on the nonlinear stage evolution of the instability: some models (Ducrocq et al. 2006, Boeuf 2014, Lafleur et al. 2016a) show a transition of the mode into the regime of the ion-sound instability typical of un-magnetized plasmas, while other models (Jahnunen et al. 2018a) suggest that the magnetic field remains important in the mechanism of the instability, electron heating, and transport. In fact, it seems that the criteria for the nonlinear resonance broadening (the only possible mechanism responsible for the destruction of cyclotron resonances and electron demagnetization in 1D) is not satisfied and the instability continues to proceed as a coherent mode driven at the main cyclotron resonance n=1 [Eq. (1)] well into the non-linear stage. Strong inverse energy cascade towards longer wavelengths was identified and it was shown that the anomalous current is dominated by the long wavelength modes. This discrepancy can be attributed to the intrinsic limitation of missing the axial coordinate: the convection of the instability (due to a finite group velocity) away from the simulation region is not correctly modelled and extra numerical collisions are induced by the re-injection method. This conclusion is supported by the fact that: (a) varying the acceleration length and/or ion drift velocity has a significant effect on the electron transport; (b) the computed cross-field mobility has very large values (one order of magnitude larger) compared with that found in a real HT. The last point is also related to the fact that the acceleration field E_z is externally imposed and kept fixed, while one expects that an increase of the local mobility would yield a decrease of the local electric field, which would reduce the drift velocity and control the possible instabilities leading to the anomalous electron transport.

The one-azimuthal models have further limitations due to their 1D nature. First, the fluctuations are expected to have a 3D structure as measurements (Tsikata et al. 2010) indicate. Secondly, short wavelength instabilities with a significantly large component along the magnetic field reduce to the unmagnetized (ion-sound) form as seen from the analytical solution of the dispersion relation. Recent models (Héron-Adam 2013, Hara-Cho 2017, Croes et al. 2017, Jahnunen et al. 2018b, Tavant et al. 2018, Taccogna et al. 2019) have added the radial coordinate resolving the direction along the magnetic field and accounting for the sheath boundary conditions. They have shown that the full ion sound regime is not realized, but a more effective regime of discrete cyclotron resonance instabilities (again inverse cascade towards low wavenumbers) occur. The magnetic field remains to be a defining feature of ExB drift instability for HT operational regime. Finally, a long wavelength modified-two-stream instability (MTSI) is also detected, responsible for alternating radial jets along the azimuthal direction.

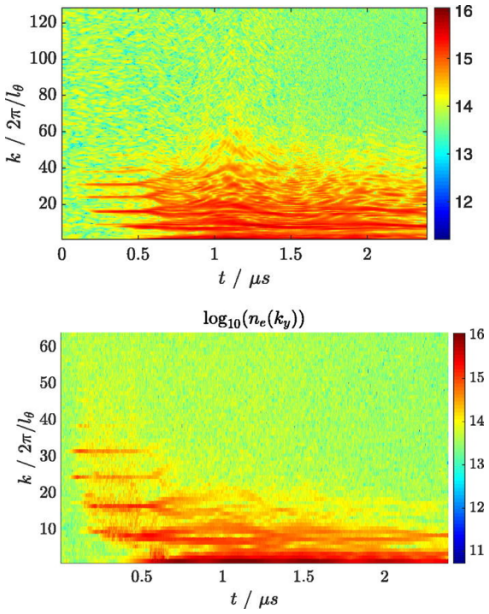

Fig. 17 Evolution of the azimuthal ion density (top) and electron density (bottom) k-spectra over time at a particular radial location between the two walls, plotted as $\log_{10}\tilde{n}_{i,e}$. Discrete peaks corresponding to the first cyclotron harmonics Eq. (35) are evident while the lowest peak (after 0.5 μs) is the MTSI mode. Results from 2D(radial, azimuthal) PIC model (Jahnunen et al. 2018b).

Another important aspect that these models can handle is the coupling between SEE and ExB EDI assessing the relative importance of these two phenomena on the electron anomalous transport. It has been recently shown (Tavant et al. 2018, Taccogna et al. 2019) that the electron radial heating due to ExB EDI can induce a larger SEE, but this, in turn, can help the ExB EDI saturation by cooling the electrons. As a result, it was observed that the anomalous electron cross-field mobility in the bulk plasma (induced by ExB EDI) decreases by 20% as the effective SEE coefficient increases. At the same time, when the SEE coefficient increases from 0 to its critical value σ_{SCS} (see Sect. 2.3), the near-wall mobility increases by a factor 2. Therefore, the total mobility is found to remain almost constant.

Finally, a regime of relaxation sheath oscillations observed in 1D-radial model (Sydorenko et al. 2009) has been also observed in the 2D(r,θ) model of Tavant et al. (2018). In particular, three regimes have been identified when varying the effective SEE coefficient. For low SEE rates, the plasma sheath at the walls has a typical monotonic spatial profile. This region is stable. For high SEE rates, a potential well is observed to form near the wall due to space charge effects associated with intense electron emission. This saturated regime is also found to be stable. However, for

intermediate SEE rates, an oscillatory behavior is observed where the potential profile changes between those for a standard monotonic sheath, and the saturated sheath.

As seen before, missing the axial coordinate is a possible candidate of discrepancies and inconsistencies among the different results obtained. 2D(θ,z) models (Adam et al. 2004, Coche and Garrigues 2014, Lafleur and Chabert 2018, Lafleur et al. 2018, Boeuf and Garrigues 2018, Katz et al. 2018, Taccogna et al. 2019), in the two possible versions (prescribed neutral or ionization source term profiles), take naturally into account the finite axial length and the wave convection, density/temperature axial gradients and axial magnetic field profile. Differently from the results obtained with some 1D(azimuthal) and 2D(azimuthal-radial) models, the scaling of wavelength ($\lambda \sim \lambda_{De}$), frequency ($\omega \sim \omega_{pi}$) and amplitude of the azimuthal field ($|E_\theta| \sim \frac{T_e}{\lambda_{De}}$|) obtained within azimuthal-axial models is consistent with an ion acoustic character of the instability.

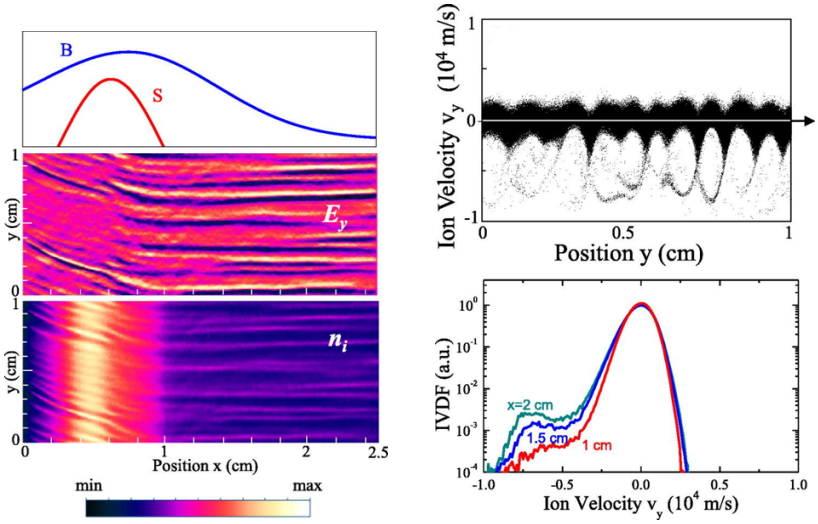

Fig. 18 On the left, two dimensional axial-azimuthal distributions of the azimuthal electric field E_y (range between -5x10^4 and 5x10^4 V/m) and of the ion density n_i (range between 0 and 5x10^{17} m^{-3}), using the axial distributions of the magnetic field and ionization rate shown on top of the contour plots. The axial and azimuthal coordinates are represented with x and y, respectively (cartesian approximation). On the right, y-v_y phase space of the ions in the last part of the discharge channel close to the exit plane (top) and ion velocity distribution function (azimuthally integrated) at three axial positions (bottom). Results from Boeuf and Garrigues (2018).

Generally speaking for all the azimuthal models, it has been shown that results are also very sensitive to the numerical parameters used. Instabilities require a very good resolution both in space/time and particle number, in order to have the modes well represented and running up to non-linear and saturation regimes. In particular, numerical noise is responsible for the destruction of electron cyclotron resonance and facilitates the transition to an ion acoustic instability. It seems that an acceptable statistical level corresponds to a number of particles per cell larger than 1000.

For two years now, a dedicated project named LANDMARK (Low temperature magnetized plasma benchmarks) has been developed to get a better understanding of non-fusion ExB plasmas (where electrons are strongly magnetized while ions are not). In particular, the project addresses physics issues related to the influence of instability and plasma-wall interaction on anomalous electron transport in ExB device and defines benchmark test cases for PIC, hybrid and fluid models.

Finally, another approach used to study the effect of azimuthal electric field on the electron trajectory is the Test Particle Monte Carlo model (Taccogna et al. 2010). It does not solve for self-consistent field as PIC method, but rather use the field characterized by PIC as input data. The study shows as the electron trajectory elongation along the axial direction towards the anode is a function of the field amplitude and that the distribution functions of jump size and waiting time (elapsed

between two successive jumps) of electron guiding centers show the presence of tails, typical of Lévy-flight transport.

3.5 3D PIC models

It is clear from previous reduced-dimensional models how results are strongly affected by missing some coordinates and how all the three coordinates non-linearly interfere among each other; in particular, it has been shown by the different 2D models that the radial dynamics (lateral sheaths with SEE) is strongly correlated with the azimuthal fluctuations and how the axial acceleration is an important saturation mechanism of the ExB EDI instability.

Curiously, the first 3D kinetic attempt to model HT, dates back to 90's by the pioneering works of Hirakawa and Arakawa (1995 and 1996) who applied PIC-MCC technique to a SPT50 using artificially small ion mass and large vacuum permittivity. Nowadays, the only 3D models are able to simulate miniaturized version of HT (Minelli and Taccogna 2018, Taccogna and Minelli 2018) and microwave ion thruster (Takao et al. 2014).

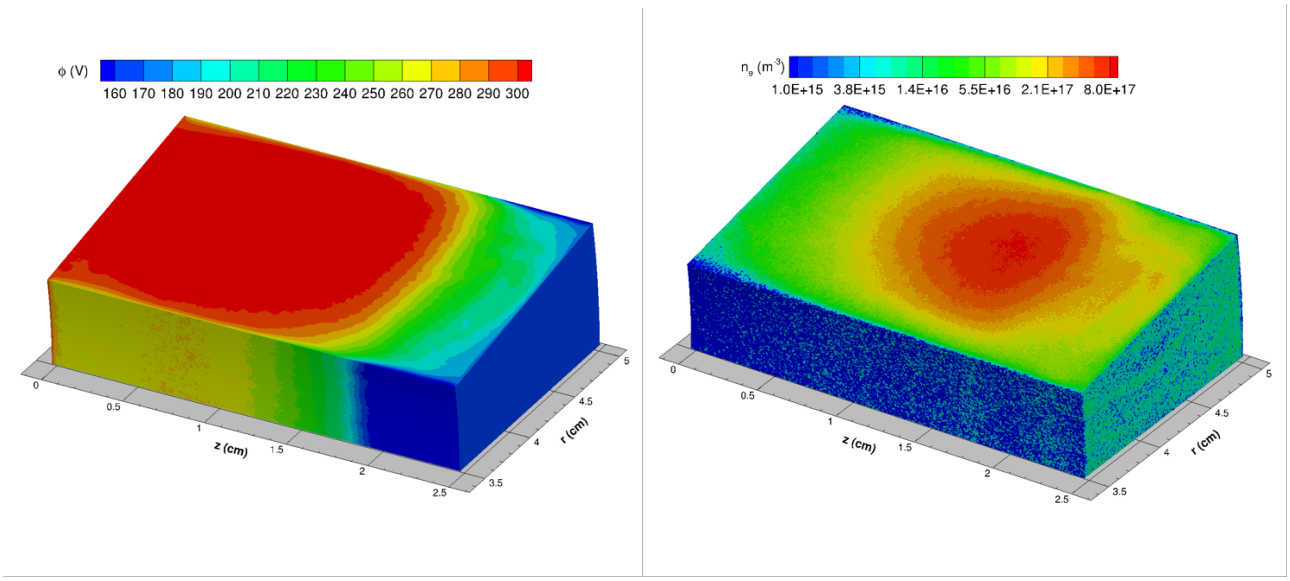

Fig. 19 Three-dimensional distributions of plasma potential (left) and electron density (right) as a result of 3D cylindrical PIC simulating one azimuthal sector ($\theta=\pi/20$, i.e. one fortieth of the total azimuthal size) of a HT discharge channel.

Another important mechanism which can induce under some operative regimes an efficient electron cross-field transport in ExB device is the rotating spoke mode (Ellison et al. 2012). It consists of an azimuthal low frequency (kHz range), high wavelength (several centimetres) ionization oscillation moving azimuthally with a phase velocity $v_{ph} \approx 0.2\frac{E_z}{B_r}$ and presents in the near-anode or near-plume regions of the discharge. It has been recently investigated by 3D PIC models (Tang et al. 2012, Matyash et al 2017).

3.6 Kinetic Models of the Plume

Several physical phenomena controlling the functioning of HTs take place in the near-field region of the plume: residual ion acceleration (one third of the potential drop occurs in the plume), anomalous electron transport from the cathode to the entrance of the channel, further ionization, ion-neutral charge exchange, ion beam neutralization, asymmetry induced by the cathode location. Therefore, understanding the plasma physics involved in this region is crucial for the improvement

and optimization of HT. Often, models developed to study this region are fluid or hybrid (Taccogna et al. 2002, 2004b, 2014b and Domínguez-Vázquez et al. 2018b, see previous Sect. 2) considering always the electrons as Maxwellian. However, due to the complexity of this transition region, and in particular to the following elements: (a) magnetic field still large enough to magnetized electrons; (b) collisions not sufficient to guarantee the equilibrium; (c) strong plasma/fields gradients; (d) non-neutrality very close to the exit plane; (e) possible secondary electron emission at the front plane of the thruster; (f) electron collision-less cooling: the electron does not follow the Boltzmann (γ=1) nor the simple adiabatic expansion (γ=5/3) relations:

$$T_e \propto n_e^{\gamma-1}. \quad (36)$$

The best fitting value of γ for SPT-100 ranges between 1.2 and 1.5 (Giono et al. 2017), indicating the existence of non-trivial kinetic heat fluxes.

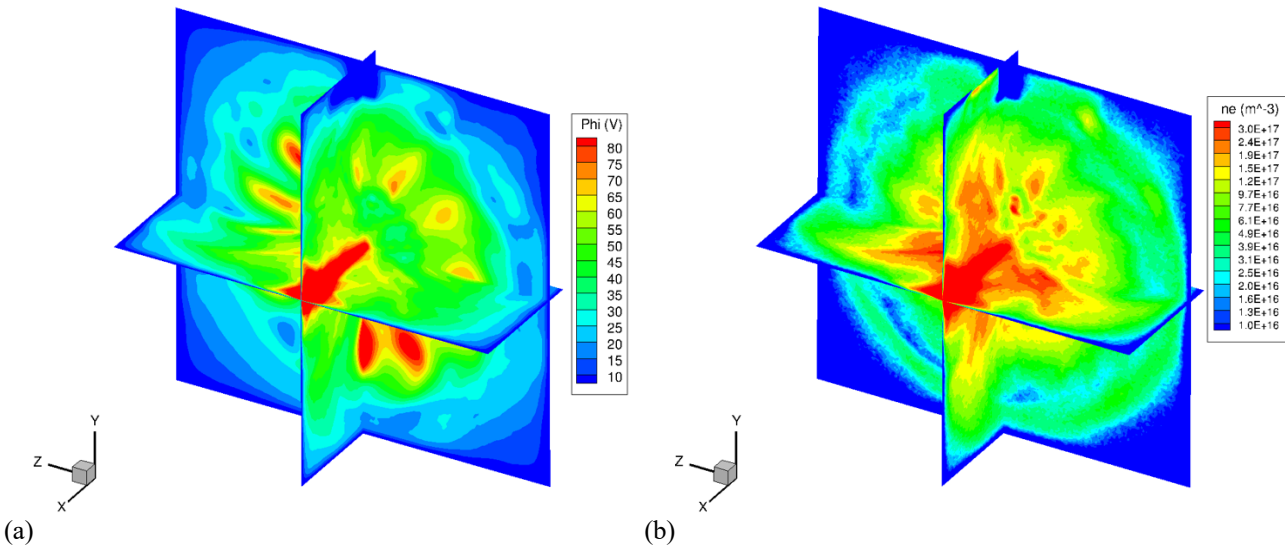

Fig. 20 Three-dimensional structure of (a) plasma potential and (b) electron density in the near-field plume region of a HT. The cathode (blue parallelepiped) is evident on the top and the axial coordinate is x.

In order to take into account these kinetic effects, three different approaches have been developed.

3D simulations of electron trajectories in a non-self-consistent electric field (obtained from plasma potential measurements) have been performed by Smith-Cappelli (2010a and 2010b) in order to better understand the near-field electron transport from the cathode to the channel entrance. They show that the three-dimensionality of the E and B fields (e.g., non-axisymmetric E or B fields), together with electron-wall collisions, appears to be important drivers of cross-field transport in this region of the discharge, and could lead to sufficient levels of electron transport to the channel without invoking plasma turbulence.

A classical self-consistent fully kinetic PIC model has been developed by Oudini et al. (2013) and Hu and Wang (2015) to investigates the very near-field region of the plume. Results show the effect of the magnetization of electrons on the plasma expansion and the importance of electron-wall interaction on the thruster exit plane. Furthermore, results evidence the presence of azimuthal fluctuations mainly in the region located between the exhaust plan and the cathode.

Finally, Merino et al. (2018) studied the problem of electron cooling in the plume treating them as unmagnetized and collisionless. The model exploits the conservation of mechanical energy and angular momentum about the plume axis, and the adiabaticity of the radial action integral, to

integrate the electron Vlasov equation. Phase space is divided into regions of four different types: free electrons, reflected electrons, empty regions, and doubly-trapped electrons.

3.7 Zero Dimensional Global and Collisional Radiative Models

A separate treatment deserves the presentation of particular kinetic approach such as global and collisional radiative (CR) models.
Global models use particle and energy balance equations to provide a volume-averaged 0D study of the discharge performance. The early versions of this model required input of the measured plasma parameters and have been developed for the magnetic ring cusp gridded ion thruster (Goebel 1982 and Brophy 1984). It was later improved by including self-consistent calculations of the neutral pressure, electron temperature, and charged particle recycling in the thruster volume (Goebel et al. 2007). Goebel (2008) adapted the global model to also study the RF ion thruster discharge. The model does not describe the power transfer from the RF generator to the plasma, and does not treat the neutral gas heating. These improvements were obtained by Chabert et al. (2012) and Grondein et al. (2016) by using atomic (Xe) and molecular (I_2) gas propellant, respectively.
CR models instead determine the exited energy states (ground and metastables) of atomic and ion population by using electron-induced excitation, de-excitation and ionization collisions, and spontaneous radiative de-excitation transitions. Often these models, developed for Ar and Xe, use Maxwell-Boltzmann energy distribution for electrons and a delta function at the nominal accelerated energy for ions (Dressler et al. 2009 and Yang et al. 2010) with a uniform, quasi-neutral and optically thin plasma. CR models are used as calibration of passive optical diagnostic to convert absolute or relative line emission intensities into plasma parameters such as the electron temperature.

4 Conclusions: the future of HT modeling

Hall Thrusters represent probably one of the richest device of low temperature plasma phenomena. This variety must naturally come to terms with a certain difficulty in characterizing HTs from a theoretical-analytical and experimental point of view. The mathematical treatment is simply impractical due to the enormous number of degrees of freedom non-linearly coupled that are involved, while experimental diagnostic techniques are often invasive, difficult to implement (inaccessibility if one wants to characterize the plume behavior into the Space environments or wants measure quantities inside the discharge channel due to the small size of some HTs), very expensive and sometime unreliable for the basic assumptions on which they are based. Therefore, it represents the typical case where computer modeling, bridge between theory and observation, shed light on the HT physics.

In the last thirty years the role of HT numerical models is continuously increased. The two main approaches, fluid and kinetic, have not only been used to gain insight and understand the complex physical mechanisms that, interacting with each other, give rise to the global HT operation, but they have also been used to predict HT performances under non-conventional configurations and discover new physical effects. Although fluid models are fast tools capable of giving a fairly faithful representation of the HT global behavior (ionization, confinement and acceleration mechanisms), they need some ad-hoc quantities to fit experimental measurements. This is due to the fact that some aspects are deeply related to the non-equilibrium character of electrons and to the development of collective self-organized micro-structures on the Debye length scale. Kinetic models have revealed the impact of the deviation of the electron energy distribution from the Maxwellian one, the non-classical regimes of the lateral sheaths (non-monotonic and dynamic), the intimate nature of micro-instabilities enhancing the electron transport across the magnetic field lines, the neutralization and cooling mechanisms in the expanding plume. Among the different

kinetic approaches, the particle-based methodology is showing as the most effective due to the fact that HT is the typical case where we know the fundamental laws that govern it, but we are simply unable to work out their consequences.

Of course, the power of this approach is directly related to the progress in computer science, high-performance computing and numerical algorithms. Future models will be able to simulate the plasma behavior in larger computational domains (moving the boundaries farther and reducing their artificial impact) spanning a larger time interval and with a better statistical level (reduction of the numerical noise due to the discrete nature of PIC model) in three dimensions. These models will be able to produce increasingly consistent results, less affected by numerical contaminations leading to real numerical experiments with a huge quantity of computed data. HT modeling will experience a transition from computationally-intensive to data-intensive problems. In this context, the coupling of predictive HT plasma models with new computational techniques (machine and deep learning, complex network theory, optimization algorithms) will lead to a new era of thruster technology where empirical methods in R&D will leave the place to more rigorous and less risky methods, in which new results, new combinations of discharge geometry, electromagnetic configuration, propellant chemistry and wall material will be directly suggested by computers through the modeling. This huge effort will require a new kind of collaboration inside the HT modeling community where many groups from different institutions will provide their skills and resources to create a common platform, widespread virtual laboratory of electric propulsion.

Acknowledgements F.T. gratefully acknowledges the invaluable help of P. Minelli, M. Capitelli, S. Longo, R. Schneider, K. Matyash, E. Ahedo, A. Domínguez-Vázquez, Z. Asadi and G. Bogopolsky. L.G. is very grateful to his colleagues J.P. Boeuf and G.J.M. Hagelaar and PhD students J. Bareilles, C. Boniface, J. Pérez Luna, and P. Coche from LAPLACE, and members of research group of Space Propulsion J.C. Adam, L. Albarède, S. Barral, S. Béchu, G. Bonhomme, A. Bouchoule, F. Darnon, F. Doveil, M. Dudeck, N. Gascon, D. Gresillon, A. Héron, P. Lasgorceix, V. Latocha, N. Lemoine, S. Mazouffre, D. Pagnon, S. Roche, S. Tsikata, and V. Vial for stimulating exchanges and numerous fruitful discussions since 1996. The constant financial support of MIUR (Ministero dell'Istruzione, dell'Università e della Ricerca) and CNES (Centre National d'Etudes Spatiales) are also acknowledged. Authors dedicate this paper to the memory of Alexey I. Morozov and Michel Dudeck.

Compliance with ethical standards

Conflict of interest statement On behalf of all authors, the corresponding author states that there is no conflict of interest.

Appendix 1: Secondary electron emission models

Secondary electron emission (SEE) induced by electron impact on dielectric surfaces is a complex phenomenon which involve elastic and inelastic scattering of electron in its transport inside the material. The emission of secondaries can also involve not only the primary electron (coming from the plasma) itself, but by an electron cascade process also electrons belonging to the material. Due to the fast timescale of the process, its implementation in PIC model can be done by a phenomenological approach. It is important to note that in PIC models the secondary electrons are generated instantaneously when a primary electron hits the surface. This assumption is well justified, since the time lag of secondary emission is estimated to be 10^{-13}-10^{-14} s, i.e., much shorter than the timestep used for PIC relevant to HT plasma parameters. The phenomenological models of SEE are based on the two main quantities representing SEE (Villemant et al. 2017): 1) the yield SEY σ, number of electrons emitted per incident electron; 2) energy and angular spectrum of

secondaries emitted $d^2\sigma/dEd\Omega$. Both are mainly functions of the incident electron energy E_p, angle of impact θ_p, wall temperature T_w and electron irradiation (aging).

The dependence of the yield from the primary electron energy follows an universal (the same for all materials) behavior that can be represented by 5 parameters: 1) σ_0 value of SEY at E_p=0; 2) maximum value of SEY σ_{max}; 3-4) first and second crossover energy E^* and E^{**} corresponding to the lower and higher, respectively, primary energy giving $\sigma(E_p)$=1; 5) incident electron energy corresponding to the maximum yield E_{max}. The following order always fulfills: $E^*<E_{max}<E^{**}$. For HT typical regimes (E_p<1 keV) and dielectric materials used, only two parameters are important, σ_0 and E^* (see Figa. 21(a-b) and Tab. III). For a given primary energy, SEY increases with increasing angle of incidence θ_p. Concerning the wall temperature and electron irradiation dependences, σ_0 decreases while E^* increases with electron irradiation and T_w (Tondu et al. 2011 and Belhaj et al. 2015), making the SEE process more negligible for hotter and highly irradiated surfaces.

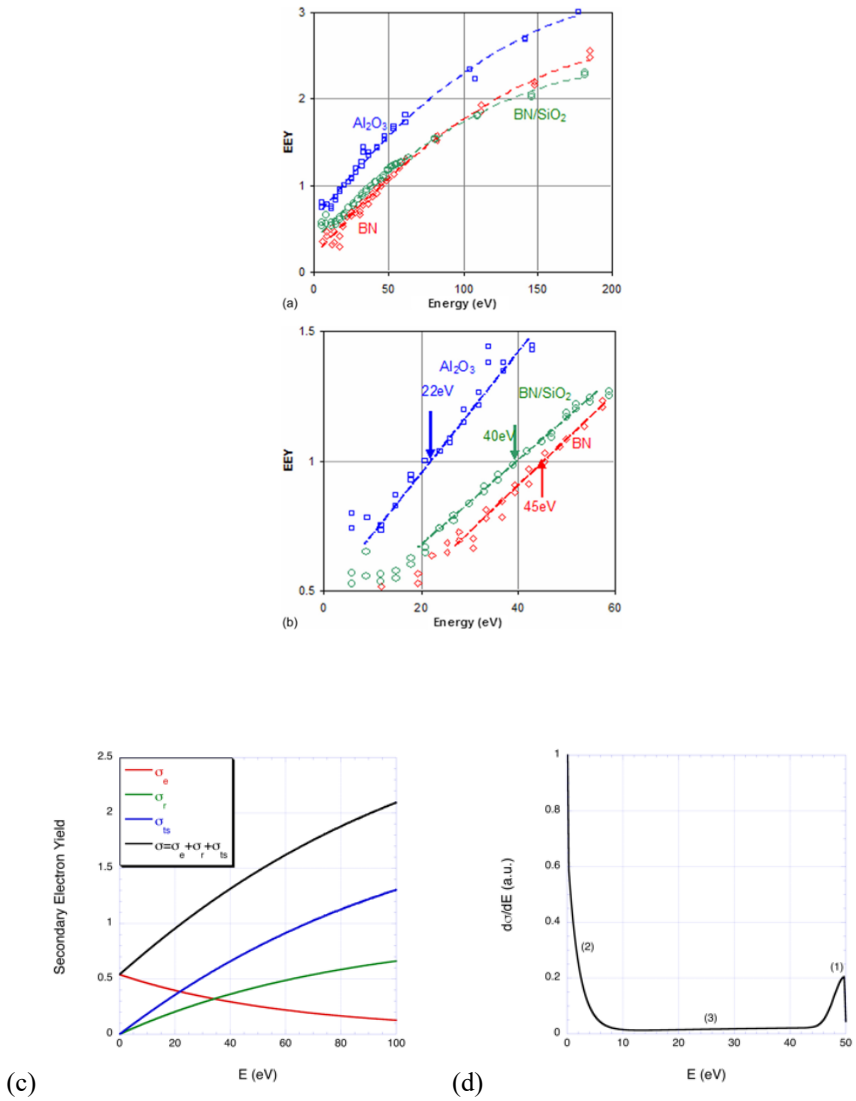

Fig. 21 (a) Total SEE yields as a function of primary electron energy (Tondu et al. 2011) for some HT wall materials with (b) zoom view around the first crossover energy (indicated with arrows). (c) Components of SEY as a function of impact electron energy and (d) energy spectrum dσ/dE of secondary electrons emitted by a beam of electrons with energy E_p=50 eV. The energy range of the three different secondary populations, (1) elastic backscattered, (2) true secondaries and (3) inelastic backscattered, is evident. SEYs and energy spectrum are computed using the Furman-Pivi (2002) model for Al_2O_3 surface.

Wall Material	σ_0	E^* (eV)
Al_2O_3	0.57	22
BN	0.24	45
SiO_2	0.5	18
$BNSiO_2$	0.54	40
SiC	0.69	43

Tab. III Typical values of SEY at E_p=0 and first crossover energy for wall materials relevant for HTs (Barral et al. 2003, Dunaevsky et al. 2003, Tondu et al. 2011 and Villemant et al. 2017).

Concerning the energy spectrum of the emitted electrons (see Fig. 21(c-d)), three different populations can be distinguished: 1) high-energy electrons corresponding to primary electrons backscattered from the surface (their energy is slightly below the incident electron energy); 2) true secondary electrons belonging to the material and representing the low-energy part of the spectrum; 3) primary electrons diffused inside the material and having suffered inelastic collisions (their energy range is between the true secondaries and the peak of backscattered electrons). The yield of each secondary electron has a proper behavior as a function of the incident energy. The backscattering and inelastic SEYs σ_e and σ_r grow with the decrease of E_p, while the yield of true secondary electrons σ_{ts} decreases and reaches zero at an energy of about the width of the potential gap between vacuum and the upper level of the valence band. Therefore, the total yield $\sigma=\sigma_e+\sigma_r+\sigma_{ts}$ could have a distinguishable minimum in the low energy region (E_p<10 eV). The angular spectrum of emitted electrons shows always an isotropic distribution over the azimuthal angle θ, while the polar angle φ has a cosine (Lambertian) distribution for true secondaries and a more complex distribution depending of the angle of impact for the elastic and inelastic backscattered electrons.

Depending on the number of parameters used, three different phenomenological models have been proposed:

1) Linear law model

It represents the simplest model where only σ_0 and E^* are used to represent the total yield following a linear relation

$$\sigma(E) = \sigma_0 + \frac{E}{E_*}(1-\sigma_0). \qquad (37)$$

All electrons are emitted with a half-Maxwellian distribution with T_{see}=2 eV. Their angular distribution is isotropic over the azimuthal angle θ and cosine law over the polar angle φ, and independent of the primary electron angle of incidence.

2) Modified Vaughan Model

It was proposed by Sydorenko (2006) and makes use of the Vaughan (1989) fitting formula

$$\sigma_{Vaug}(E,\theta) = \sigma_{max}(\theta)\left[v(E,\theta)e^{1-v(E,\theta)}\right]^k \quad (38)$$

where $v(E,\theta) = \frac{E-E_0}{E_{max}(\theta)-E_0}$, $E_{max}(\theta) = E_{max,0}\left(1+\frac{k}{\pi}\theta^2\right)$, $\sigma_{max}(\theta) = \sigma_{max,0}\left(1+\frac{k}{\pi}\theta^2\right)$ and $k = \begin{cases} 0.62 & E < E_{max} \\ 0.25 & E > E_{max} \end{cases}$, to define the partial yields for the different secondaries:

$$\sigma_e(E,\theta) = r_e\sigma_{Vaug}(E,\theta) + \sigma_{e,max}\begin{cases} v_1(E)e^{1-v_1(E)} & E_{e,0} < E < E_{e,max} \\ [1+v_2(E)]e^{-v_2(E)} & E > E_{e,max} \end{cases} \quad (39.a)$$

$$\sigma_r(E,\theta) = r_r\sigma_{Vaug}(E,\theta) \quad (39.b)$$

$$\sigma_{ts}(E,\theta) = (1-r_e-r_r)\sigma_{Vaug}(E,\theta) \quad (39.c)$$

where $v_1(E) = \frac{E-E_{e,0}}{E_{e,max}-E_{e,0}}$ and $v_2(E) = \frac{E-E_{e,max}}{\Delta}$.

The energy spectrum of secondaries is prescribed as follows: the backscattered electrons keep the primary energy, the energy of inelastically backscattered electrons is considered to be uniformly distributed between zero and the energy of the incident electron and the true secondaries are emitted with a half-Maxwellian distribution with T_{see}=2 eV. The same angular spectrum of the linear model is used.

The total number of parameters used is 9 and their values for BN are reported in Tab. IV.

E_0 (eV)	k	$\sigma_{max,0}$	$E_{max,0}$ (eV)	r_e	$E_{e,0}$	$\sigma_{e,max}$	$E_{e,max}$ (eV)	r_i
13	1	3	500	0.03	2	0.55	10	0.07

Tab. IV Parameters used in the Modified Vaughan Model for BN material.

3) Furman-Pivi Model

It represents the most sophisticated SEE model able to fit in detail the three partial SEY behaviors as a function of impact energy and angle (with the possibility of emission of n>1 secondaries) (Furman and Pivi 2002). The three yields for normal incidence (in Fig. 21(b) is reported their behavior for BN in the energy range 0-100 eV) are

$$\sigma_e(E,0) = \sigma_{e,\infty} + \left(\sigma_0 - \sigma_{e,\infty}\right)e^{-E/E_e} \quad (40.a)$$

$$\sigma_r(E,0) = \sigma_{r,\infty} + \left(1 - e^{-E/E_r}\right) \quad (40.b)$$

$$\sigma_{ts}(E,0) = \frac{\sigma_{max}sE'}{(s-1+E'^s)\left(1-\sigma_e(E,0)-\sigma_r(E,0)\right)} \quad (40.c)$$

where E'=E/E_{max}. The incident-angle dependence is implemented assuming the same form for all three components of SEY. Specifically, for the backscattered and redifussed components

$$\sigma_e(E,\theta) = \sigma_e(E,0)[1 + e_1(1 - cose^{e_2}\theta)] \quad (41.a)$$

$$\sigma_r(E,\theta) = \sigma_r(E,0)[1 + r_1(1 - cose^{r_2}\theta)] \quad (41.b)$$

and for the true-secondary component

$$\sigma_{ts}(E,\theta) = \sigma_{ts}(E,0)[1 + t_1(1 - cose^{t_2}\theta)] \quad (41.c)$$

$$E'(E,\theta) = E'(E,0)[1 + t_3(1 - cose^{t_4}\theta)] \quad (41.d)$$

The emitted energy (see Fig. 21(c)) and angular spectrum are also functions of impact energy and angle and their calculation requires a complex implementation [see Furman and Pivi (2002) for details]. This precision is at the expense of the computational complexity and the high number of free parameters (42) necessary to implement the model and that makes it not very useful for a parametric study of the effect of the walls on the plasma behavior inside HT.

Appendix 2: Ion Erosion model

One critical issue of Hall thruster is the wall erosion since with the existence of a radial electric field inside the channel, ions generate downstream interact with walls (see Sect. 2.5). The erosion rate in eroded thickness by units of time can be expressed as:

$$R = \frac{m_{\mathrm{w}}}{\mathcal{N}_a \rho_{\mathrm{w}}} \Gamma_{i,\perp} Y(\varepsilon_{i,\mathrm{w}}, \theta_{i,\mathrm{w}}), \tag{42}$$

where the properties of the wall materials are characterized through mass m_w and mass density ρ_w, $\mathcal{N}_a$ is the Avogadro's number, and $\Gamma_{i,\perp}$ is the incident ion flux including multi-charged ions. The contribution of unionized propellant atoms on sputtering processes is found to be minor (Sommier et al. 2005). The function Y is the sputtering yield (number of atoms sputtered by incident ions) and depends on the ion impact energy $\varepsilon_{i,\mathrm{w}}$ and angle $\theta_{i,\mathrm{w}}$. The energy of ions impinging the walls is the sum of the ion energy gained in the plasma before the sheath entrance and a supplementary energy resulting from the sheath potential drop (see Sect. 2.3). Obviously, for fluid description of ions, additional assumption about the ion energy distribution at the sheath entrance must be done. The function Y can be a complex function depending on energy and angle and is most of time split in two separated functions:

$$Y\left(\varepsilon_{i,\mathrm{w}}, \theta_{i,\mathrm{w}}\right) = Y_\varepsilon\left(\varepsilon_{i,\mathrm{w}}\right) Y_\theta\left(\theta_{i,\mathrm{w}}\right), \tag{43}$$

where Y_ε determines the energy dependence at normal incidence and Y_θ acts as a correcting factor to account for angle incidence effect. There is a large uncertainty associated to the sputtering yield for energies of interest in the context of Hall thrusters (between few tens to few hundreds of eV). Most of time semi-analytical laws coming from the original work of Yamamura and Tarawa (1996) for monoatomic solids are used in which parameters are adjusted to fit measurements of sputtering yield at normal incidence for high energy ions. For BN material, measurements are taken from works of Garnier et al. (1999) and Yalin et al. (2007). Fig. 22 shows the Y_θ and Y_ε analytical fitting curves in the context of the study of the 6 kW H6 thruster with BN walls. The Yamamura and Tarawa formulation have been completed with additional functions based on works of Bohdansky (1984) where an additional parameter linked to the sputtering energy threshold $Y_{\varepsilon,th}$ (unknown) appears. In sputtering models, under the $Y_{\varepsilon,th}$ limit, $Y_\varepsilon = 0$. Mikellides and co-workers found that $Y_{\varepsilon,th}$ taken in the 25 eV to 50 eV range is a reasonable choice to match measurements at high energy (Mikellides et al. 2014a). In the study of the SPT100 with $BNSiO_2$ wall material, Garrigues and co-workers have fixed the unknown sputtering energy threshold between 30 and 70 eV (Garrigues et al. 2003).
An extensive review on ion erosion models can be found in Boyd and Falk (2001).

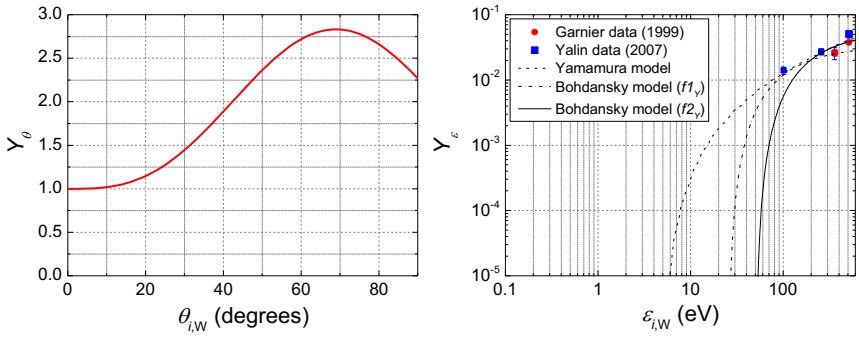

Fig. 22 Analytical fitting curves (left) angular, (right) energy dependencies of sputtering yield for BN walls. $f1_Y$ and $f2_Y$ fitting functions assuming a sputtering energy threshold of 25 eV and 50 eV, respectively (from Mikellides et al. 2014a).

Appendix 3: Poisson equation solvers

Usually in HT PIC models the electrostatic approximation is used: the current involved are quite low to change the externally imposed magnetic field. The generalized form of Poisson Eq. () which can take into account the change of the dielectric permittivity across the boundary between plasma channel and lateral dielectric surfaces, takes the following form:

$$\nabla \cdot (\epsilon \nabla \phi) = -\rho. \qquad (44)$$

After discretization it leads to a system of linear equations

$$\boldsymbol{A}\phi = \boldsymbol{b} \qquad (45)$$

where $\boldsymbol{A}$ is a matrix containing the information on the geometry used and of the boundary conditions. The latter can be of two types: Dirichelet conditions (fixed electric potential) as at the anode and cathode location and Neumann conditions (fixed electric potential derivative) as at the outflow in the plume region. In three-dimension model $\boldsymbol{A}$ can be a very large and sparse matrix and the direct inversion is a difficult solver option. Relaxation methods can be often applied to iteratively find the solution. Nowadays different fast numerical free software package are available as Poisson's equation solver: HYPRE, FISHPACK, SuperLU, PETSc and WSMP.

References

J.C. Adam, A. Héron, G. Laval, Study of stationary plasma thrusters using two-dimensional fully kinetic simulations, Phys. Plasmas **11**, 295 (2004). doi: 10.1063/1.1632904

E. Ahedo, P. Martínez-Cerezo, M. Martínez-Sanchez, One-dimensional model of the plasma flow in a Hall thruster, Phys. Plasmas **8**, 3058 (2001). doi: 10.1063/1.1371519

E. Ahedo, J.M. Gallardo, M. Martínez-Sánchez, Model of the plasma discharge in a Hall thruster with heat conduction, Phys. Plasmas **9**, 4061 (2002). doi: 10.1063/1.1499496

E. Ahedo, Presheath/sheath model with secondary electron emission from two parallel walls, Phys. Plasmas **9**, 4340 (2002). doi: 10.1063/1.1503798

E. Ahedo, J.M. Gallardo, M. Martínez-Sánchez, Effects of the radial plasma-wall interaction on the Hall thruster discharge, Phys. Plasmas **10**, 3397 (2003). doi: 10.1063/1.1584432

E. Ahedo, V. De Pablo, Combined effects of electron partial thermalization and secondary emission in Hall thruster discharges, Phys. Plasmas **14**, 083501 (2007). doi: 10.1063/1.2749237

E. Ahedo, R. Santos, F. I. Parra, Fulfillment of the kinetic Bohm criterion in a quasineutral particle-in-cell model, Phys. Plasmas **17**, 073507 (2010). doi: 10.1063/1.3456516

E. Ahedo, Plasmas for space propulsion, Plasma Phys. Control. Fusion **53**, 124037 (2011). doi: 10.1088/0741-3335/53/12/124037

T. Andreussi, V. Giannetti, A. Leporini, M. M. Saravia, M. Andrenucci, Influence of the magnetic field configuration on the plasma flow in Hall thrusters, Plasma Phys. Control. Fusion **60**, 014015 (2018). doi: 10.1088/1361-6587/aa8c4d

J. Askenazy, A. Fruchtman, Y. Raitses, N.J. Fish, Modelling the behaviour of a Hall current plasma accelerator, Plasma Phys. Control. Fusion **41**, A357 (1999). doi: 10.1088/0741-3335/41/3A/029

J. Bareilles, G.J.M. Hagelaar, L. Garrigues, C. Boniface, J.P. Boeuf, N. Gascon, Critical assessment of a two-dimensional hybrid Hall thruster model: Comparisons with experiments, Phys. Plasmas **10**, 4886 (2003). doi: 10.1063/1.1719022

S. Barral, K. Makowski, Z. Peradzynski, N. Gascon, M. Dudeck, Wall material effects in stationary plasma thrusters.II. Near-wall and in-wall conductivity, Phys. Plasmas **10**, 4137 (2003). doi: 10.1063/1.1611881

M. Belhaj, K. Guerch, P. Sarrailh, N. Arcis, Temperature effect on the electron emission and charging of BN–SiO2 under low energy electron irradiation Nucl. Instrum. Meth. Phys. Res. B **362**, 163 (2015). doi: 10.1016/j.nimb.2015.09.082

C.K. Birdsall, A.B. Langdon, *Plasma physics via computer simulation* (Taylor and Francis, 2005)

J. A. Bittencourt, *Fundamentals of plasma physics*, third edition, Springer, New York (2004)

J.P. Boeuf, L. Garrigues, Low frequency oscillations in a stationary plasma thruster, J. Appl. Phys. **84**, 3541 (1998). doi: 10.1063/1.368529.

J. P. Boeuf, Rotating structures in low temperature magnetized plasmas—insight from particle simulations, Front. Phys. **2**, 74 (2014). doi: 10.3389/fphy.2014.00074

J.P. Boeuf, Tutorial: Physics and modeling of Hall thrusters, J. Appl. Phys. **121**, 011101 (2017). doi: 10.1063/1.4972269

J.P. Boeuf, L. Garrigues, ExB electron drift instability in Hall thrusters: Particle-in-cell simulations vs. theory, Phys. Plasmas **25**, 061204 (2018). doi: 10.1063/1.5017033

J. Bohdansky, A universal relation for the sputtering yield of monatomic solids at normal ion incidence, Nucl. Instrum. Meth. B **2**, 587 (1984). doi: 10.1016/0168-583X(84)90271-4

A. Bouchoule, C. Philippe-Kadlec, M. Prioul, F. Darnon, M. Lyszyk, L. Magne, D. Pagnon, S. Roche, M. Touzeau, S. Béchu, P. Lasgorceix, N. Sadeghi, N. Dorval, J.P. Marque, J. Bonnet, Transient phenomena in closed electron drift plasma thrusters: insights obtained in a French cooperative program, Plasma Sources Sci. Technol. **10**, 364 (2001). doi: 10.1088/0963-0252/10/2/326

I.D. Boyd, M.L. Falk, A review of spacecraft material sputtering by Hall thruster plumes, 37th Joint AIAA/ASME/SAE/ASEE Propulsion Conference and Exhibit (American Institute of Aeronautics and Astronautics, Salt Lake City, UT) AIAA paper 2001-3353 (2001)

J.R. Brophy, *Ion thruster performance model*, NASA CR-174810, Ph.D. dissertation, Colorado State University (1984)

A.I. Bugrova, A.V. Desyatskov, A.I. Morozov, Electron distribution function in Hall accelerator, Sov. J. Plasma Phys. **18**, 501 (1992)

M.D. Campanell, A.V. Khrabrov, I.D. Kaganovich, General cause of sheath instability identified for low collisionality plasmas in devices with secondary electron emission, Phys. Rev. Lett. **108**, 235001 (2012). doi: 10.1103/PhysRevLett.108.235001

M.D. Campanell, A.V. Khrabrov, I.D. Kaganovich, Absence of Debye sheaths due to secondary electron emission, Phys. Rev. Lett. **108**, 255001 (2012). doi: 10.1103/PhysRevLett.108.255001

M.D. Campanell, A.V. Khrabrov, I.D. Kaganovich, Instability, collapse, and oscillation of sheaths caused by secondary electron emission, Phys. Plasmas **19**, 123513 (2012). doi: 10.1063/1.4773195

M.D. Campanell, H. Wang, Influence of emitted electrons transiting between surfaces on plasma- surface interaction, Appl. Phys. Lett. **103**, 104104 (2013). doi: 10.1063/1.4820352

M.D. Campanell H. Wang, I. D. Kaganovich, A. V. Khrabrov, Self-amplication of electrons emitted from surfaces in plasmas with ExB fields, Plasma Sources Sci. Technol. **24**, 034010 (2015). doi: 10.1088/0963-0252/24/3/034010

M.A. Cappelli, C.V. Young, A. Cha, E. Fernandez, A zero-equation turbulence model for two-dimensional hybrid Hall thruster simulations, Phys. Plasmas **22**, 114505 (2015). doi: 10.1063/1.4935891

P. Chabert, J. Arancibia Monreal, J. Bredin, L. Popelier, A. Aanesland, Global model of a gridded-ion thruster powered by a radiofrequency inductive coil, Phys. Plasmas **19**, 073512 (2012). doi: 10.1063/1.4737114

S.Y. Cheng, M. Martínez-Sanchez, Hybrid Particle-in-Cell erosion modeling of two Hall thrusters, J. Propul. Power **24**, 987 (2008). doi: 10.2514/1.36179

E.Y. Choueiri, Plasma oscillations in Hall thrusters, Phys. Plasmas **8**, 1411 (2001). doi: 10.1063/1.1354644

P. Coche, L. Garrigues, A two-dimensional (azimuthal-axial) particle-in-cell model of a Hall thruster, Phys. Plasmas **21**, 023503 (2014). doi: 10.1063/1.4864625

R.W. Conversano, D.M. Goebel, R.R. Hofer, I.G. Mikellides, R. E. Wirz, Performance analysis of a low-power magnetically shielded Hall thruster: experiments, J. Propul. Power **33**, 975 (2017a). doi: 10.2514/1.B36230

R.W. Conversano, D.M. Goebel, I.G. Mikellides, R.R. Hofer, R.E. Wirz, Performance analysis of a low-power magnetically shielded Hall Thruster: computational modeling, J. Propul. Power **33**, 992 (2017b). doi: 10.2514/1.B36231

V. Croes, T. Lafleur, Z. Bonaventura, A. Bourdon, P. Chabert, 2D particle-in-cell simulations of the electron drift instability and associated anomalous electron transport in Hall-effect thrusters, Plasma Sources Sci. Technol. **26**, 034001 (2017). doi: 10.1088/1361-6595/aa550f

F. Darnon, L. Garrigues, J.P. Boeuf, A. Bouchoule, M. Lyszyk, Spontaneous oscillations in a Hall thruster, IEEE Trans. Plasma Science **27**, 98 (1999). doi: 10.1109/27.763063

A. Domínguez-Vázquez, F. Taccogna, E. Ahedo, Particle modeling of radial electron dynamics in a controlled discharge of a Hall thruster, Plasma Sources Sci. and Technol. **27**, 064006 (2018a). doi: 10.1088/1361-6595/aac968

A. Domínguez-Vázquez, F. Cichocki, M. Merino, P. Fajardo, E. Ahedo, Axisymmetric plasma plume characterization with 2D and 3D particle codes, Plasma Sources Sci. Technol. **27**, 104009 (2018b). doi: 10.1088/1361-6595/aae702

N. Dorval, J. Bonnet, J.P. Marque, E. Rosencher, S. Chable, F. Rogier, P. Lasgorceix, Determination of the ionization and acceleration zones in a stationary plasma thruster by optical spectroscopy study: Experiments and model, J. Appl. Phys. **91**, 4811 (2002). doi: 10.1063/1.1458053

R.A. Dressler, Yu-H. Chiu, O. Zatsarinny, K. Bartschat, R. Srivastava, L. Sharma, Near-infrared collisional radiative model for Xe plasma electrostatic thrusters: the role of metastable atoms, J. Phys. D: Appl. Phys. **42**, 185203 (2009). doi: 10.1088/0022-3727/42/18/185203

A. Ducrocq, J.C. Adam, A. Héron, G. Laval, High-frequency electron drift instability in the cross-field configuration of Hall thrusters, Phys. Plasmas **13**, 102111 (2006). doi: 10.1063/1.2359718

A. Dunaevsky, Y. Raitses, N.J. Fisch, Secondary electron emission from dielectric materials of a Hall thruster with segmented electrodes, Phys. Plasmas **10(6)**, 2574 (2003). doi: 10.1063/1.1568344

C.L. Ellison, Y. Raitses, N.J. Fisch, Cross-field electron transport induced by a rotating spoke in a cylindrical Hall thruster, Phys. Plasmas **19**, 013503 (2012). doi: 10.1063/1.3671920

V.Yu. Fedotov, A.A. Ivanov, G. Guerrini, A.N. Vesselovzorov, M. Bacal, On the electron energy distribution function in a Hall-type thruster, Phys. Plasmas **6**, 4360 (1999). doi: 10.1063/1.873700

J.M. Fife, Hybrid-PIC modeling and electrostatic probe survey of Hall thrusters, Ph.D. thesis, Department of Aeronautics and Astronautics, Massachusetts Institute of Technology (1998)

FISHPACK, efficient fortran subprograms for the solution of separable elliptic partial differential equations, https://www2.cisl.ucar.edu/resources/legacy/fishpack

M.A. Furman, M.T.F. Pivi, Probabilistic model for the simulation of secondary electron emission, Phys. Rev. Special Topics-Accel. and Beams **5**, 124404 (2002). doi: 10.1103/PhysRevSTAB.5.124404

Y. Garnier, V. Viel, J.F. Roussel, J. Bernard, Low-energy xenon ion sputtering of ceramics investigated for stationary plasma thrusters, J. Vac. Sci. Technol. A **17**, 3246 (1999). doi: 10.1116/1.582050

L. Garrigues, G.J.M. Hagelaar, J. Bareilles, C. Boniface, J.P. Boeuf, Model study of the influence of the magnetic field configuration on the performance and lifetime of a Hall thruster, Phys. Plasmas **10**, 4886 (2003). doi: 10.1063/1.1622670

L. Garrigues, G.J.M. Hagelaar, C. Boniface, J.P. Boeuf, Anomalous conductivity and secondary electron emission in Hall effect thrusters, J. Appl. Phys. **100**, 123301 (2006). doi: 10.1063/1.2401773

L. Garrigues, J. Pérez Luna, J.Lo, G.J.M. Hagelaar, J.P. Boeuf, S. Mazouffre, Empirical electron cross-field mobility in a Hall effect thruster, Appl. Phys. Lett. **95**, 141501 (2009). doi: 10.1063/1.3242336

L. Garrigues, P. Coche, Electric propulsion: comparisons between Different Concepts, Plasma Phys. Control. Fusion **53**, 124011 (2011). doi: 10.1088/0741-3335/53/12/124011

L. Garrigues, Ion properties in a Hall current thruster operating at high voltage, J. Appl. Phys **119**, 163305 (2016). doi: 10.1063/1.4947523

L. Garrigues, S. Santhosh, L. Grimaud, S. Mazouffre, Operation of a low-power Hall thruster: comparison between magnetically unshielded and shielded configuration, to appear in Plasma Sources Sci. Technol. (2019).

N. Gascon, M. Dudeck, S. Barral, Wall material effects in stationary plasma thrusters.I. Parametric studies of an SPT-100, Phys. Plasmas **10**, 4123 (2003). doi: 10.1063/1.1611880

G. Giono, J.T. Gudmundsson, N. Ivchenko, S. Mazouffre, K. Dannenmayer, D. Loubère, L. Popelier, M. Merino, G. Olentšenko, Non-Maxwellian electron energy probability functions in the plume of a SPT-100 Hall thruster, Plasma Sources Sci. Technol. **27**, 015006 (2018). doi: 10.1088/1361-6595/aaa06b

D.M. Goebel, Ion source discharge performance and stability, Phys. Fluids **25**, 1093 (1982). doi: 10.1063/1.863842

D.M. Goebel, R.E. Wirz, I. Katz, Analytical ion thruster discharge performance model, J. Propuls. Power 23(5), 1055-1067 (2007). doi: 10.2514/1.26404

D.M. Goebel, Analytical discharge model for RF ion thrusters, IEEE Trans. Plasma Sci. **36**, 2111 (2008). doi: 10.1109/TPS.2008.2004232

D.M. Goebel, I. Katz, Fundamentals of electric propulsion: Hall and ion thrusters, John Wiley & Sons, Hoboken, (2008)

L. Grimaud, S. Mazouffre, Ion behavior in low-power magnetically shielded and unshielded Hall thrusters, Plasma Sources Sci. Technol. **26**, 055020 (2017a). doi: 10.1088/1361-6595/aa660d

L. Grimaud, S. Mazouffre, Conducting wall Hall thrusters in magnetic shielding and standard configurations, J. Appl. Phys. **122**, 033305 (2017b). doi: 10.1063/1.4995285

P. Grondein, T. Lafleur, P. Chabert, A. Aanesland, Global model of an iodine gridded plasma thruster, Phys. Plasmas **23**, 033514 (2016). doi: 10.1063/1.4944882

G. Guerrini, C. Michaut, M. Dudeck, A.N. Vesselovzorov, M. Bacal, Characterization of plasma inside the SPT-50 channel by electrostatic probes, 25th International Electric Propulsion Conference (The Electric Rocket Propulsion Society, Cleveland, OH) paper no IEPC-97-53 (1997)

J.M. Haas, A.D. Gallimore, Internal plasma potential profiles in a laboratory-model Hall thruster, Phys. Plasmas **8**, 652 (2001). doi: 10.1063/1.1338535

G.J.M. Hagelaar, J. Bareilles, L. Garrigues, J.P. Boeuf, Two-dimensional model of a stationary plasma thruster, J. Appl. Phys. **91**, 5592 (2002). doi: 10.1063/1.1465125

G.J.M. Hagelaar, G. Fubiani, J. P. Boeuf, Model of an inductively coupled negative ion source: I. General model description, Plasma Sources Sci. Technol. **20**, 015001 (2011). doi: 10.1088/0963-0252/20/1/015001

G.J.M. Hagelaar, Modeling of magnetized low temperature plasmas, Von Karman Institute for Fluid Dynamics, STO-AVT-VKI Lecture series 263, Electric propulsion systems, Brussels, 2016 (personal communication)

T. Hahm, Physics behind transport barrier theory and simulations, Plasma Phys. Control. Fusion **44**, A87 (2002). doi: 10.1088/0741-3335/44/5A/305

K. Hara, I.D. Boyd, V.I. Kolobov, One-dimensional hybrid-direct kinetic simulation of the discharge plasma in a Hall thruster, Phys. Plasmas **19**, 113508 (2012). doi: 10.1063/1.4768430

K. Hara, M.J. Sekarak, I.D. Boyd, A.D. Gallimore, Mode transition of a Hall thruster discharge plasma, J. Appl. Phys. **115**, 203304 (2014). doi: 10.1063/1.4879896

K. Hara, S. Cho, Radial-azimuthal particle-in-cell simulation of a Hall effect thruster, 35th International Electric Propulsion Conference (The Electric Rocket Propulsion Society, Atlanta, GE) paper no IEPC-2017-495 (2017)

W.A. Hargus Jr., C.S. Charles, Near exit plane velocity field of a 200-Watt Hall Thruster, J. Propul. Power **24**, 127 (2008). doi: 10.2514/1.29949

A. Héron, J.C. Adam, Anomalous conductivity in Hall thrusters: Effects of the non-linear coupling of the electron-cyclotron drift instability with secondary electron emission of the walls, Phys. Plasmas **20**, 082313 (2013); doi: 10.1063/1.4818796

M. Hirakawa, Y. Arakawa, Particle simulation of plasma phenomena in Hall thrusters, 24th International Electric Propulsion Conference (The Electric Rocket Propulsion Society, Moscow, Russia) paper no IEPC-1995-164 (1995)

M. Hirakawa, Y. Arakawa, Numerical simulation of plasma particle behavior in a Hall thruster, 32nd Joint AIAA/ASME/SAE/ASEE Propulsion Conference and Exhibit (American Institute of Aeronautics and Astronautics, Lake Buena Vista, FL) AIAA paper 1996-3195 (1996)

G.D. Hobbs, J.A. Wesson, Heat flow through a Langmuir sheath in the presence of electron emission, Plasma Phys. **9**, 85 (1967). doi:10.1088/0032-1028/9/1/410.

R.W. Hockney, J.W. Eastwood, *Computer simulation using particles* (IOP Publishing Ltd, 1989)

R.R. Hofer, S.E. Cusson, R.B. Lobbia, A.D. Gallimore, The H9 magnetically shielded Hall thruster, 35th International Electric Propulsion Conference (The Electric Rocket Propulsion Society, Atlanta, GE) paper no IEPC-2017-32 (2017)

Y. Hu, J. Wang, Electron properties in collisionless mesothermal plasma expansion: fully kinetic simulations, IEEE Trans. Plasma Sci. **43**, 2832 (2015). doi: 10.1063/1.4978484

HYPRE, High performance preconditioners, http://computation.llnl.gov/project/linear_solvers/software.php

R.G. Jahn, *Physics of Electric Propulsion*, Dover, New York (2006)

G.S. Janes, R.S. Lowder, Anomalous electron diffusion and ion acceleration in a low-density plasma, Phys. Fluids **9**, 1115 (1966); doi: 10.1063/1.1761810

S. Janhunen, A. Smolyakov, O. Chapurin, D. Sydorenko, I. Kaganovich, Y. Raitses, Nonlinear structures and anomalous transport in partially magnetized ExB plasmas, Phys. Plasmas **25**, 011608 (2018). doi: 10.1063/1.5001206

S. Janhunen, A. Smolyakov, D. Sydorenko, M. Jimenez, I. Kaganovich, Y. Raitses, Evolution of the electron cyclotron drift instability in two-dimensions, Phys. Plasmas **25**, 082308 (2018). doi: 10.1063/1.5033896

L. Jolivet, J.F. Roussel, Effects of secondary electron emission on the sheath phenomenon in a Hall thruster, 3rd International Conference on Spacecraft Propulsion, ESA SP-465, Cannes (France), 367-376 (2000)

B. Jorns, Predictive, data-driven model for the anomalous electron collision frequency in a Hall effect thruster, Plasma Sources Sci. Technol. **27**, 104007 (2018). doi: 10.1088/1361-6595/aae472

I.D. Kaganovich, Y. Raitses, D. Sydorenko, A. Smolyakov, Kinetic effects in a Hall thruster discharge, Phys. Plasmas **14**, 057104 (2007). doi: 10.1063/1.2709865

D. Kahnfeld, R. Heidemann, J. Duras, P. Matthias, G. Bandelow, K. Lüskow, S. Kemnitz, K. Matyash, R. Schneider, Breathing modes in HEMP thrusters, Plasma Sources Sci. Technol. **27**, 124002 (2018). doi: 10.1088/1361-6595/aaf29a

I. Katz, I. G. Mikellides, Neutral gas free molecular flow algorithm including ionization and walls for use in plasma simulations, J. Comput. Phys. **230**, 1454 (2011). doi: 10.1016/j.jcp.2010.11.013

I. Katz, H. Chaplin, A. Lopez Ortega, Particle-in-cell simulations of Hall thruster acceleration and near plume regions, Phys. Plasmas **25**, 123504 (2018). doi: 10.1063/1.5054009

M. Keidar, I.D. Boyd, I.I. Beilis, Plasma flow and plasma–wall transition in Hall thruster channel, Phys. Plasmas **8**, 5315 (2001). doi: 10.1063/1.1421370

M. Keidar, I.D. Boyd, I.I. Beilis, Modeling of a high-power thruster with anode layer, Phys. Plasmas **11**, 1715 (2004). doi: 10.1063/1.1668642

H. Koizumi, K. Komurasaki, Y. Arakawa, Numerical prediction of wall erosion on a Hall thruster, Vacuum **83**, 307 (2008). doi: 10.1016/j.vacuum.2008.03.096

K. Komurasaki, Y. Arakawa, Two-dimensional model of plasma flow in Hall thruster, J. Propul. Power **11**, 1317 (1995). doi: 10.2514/3.23974

J.W. Koo, I.A. Boyd, Computational model of a Hall thruster, Comput. Phys. Commun. **164**, 442 (2004). doi: 10.1016/j.cpc.2004.06.058

N.A. Krall, A.W. Trivelpiece, *Principles of Plasma Physics*, McGraw-Hill, New York, (1973)

I. Kronhaus, A. Kapulkin, M. Guelman, B. Natan, Investigation of two discharge configurations in the CAMILA Hall thruster by the particle-in-cell method, Plasma Sources Sci. Technol. **21**, 035005 (2012). doi:10.1088/0963-0252/21/3/035005

T. Lafleur, S.D. Baalrud, P. Chabert, Theory for the anomalous electron transport in Hall effect thrusters. I. Insights from particle-in-cell simulations, Phys. Plasmas **23**, 053502 (2016a). doi: 10.1063/1.4948495

T. Lafleur, S.D. Baalrud, P. Chabert, Theory for the anomalous electron transport in Hall effect thrusters. II. Kinetic model, Phys. Plasmas **23**, 053503 (2016b). doi: 10.1063/1.4948496

T. Lafleur, S.D. Baalrud, P. Chabert, Characteristics and transport effects of the electron drift instability in Hall-effect thrusters, Plasma Sources Sci. Technol. **26**, 024008 (2017). doi: 10.1088/1361-6595/aa56e2

T. Lafleur, P. Chabert, The role of instability-enhanced friction on 'anomalous' electron and ion transport in Hall-effect thrusters, Plasma Sources Sci. Technol. **27**, 015003 (2018). doi: 10.1088/1361-6595/aa9efe

T. Lafleur, R. Martorelli, P. Chabert, A. Bourdon, Anomalous electron transport in Hall-effect thrusters: Comparison between quasi- linear kinetic theory and particle-in-cell simulations, Phys. Plasmas **25**, 061202 (2018). doi: 10.1063/1.5017626

C.M. Lam, E. Fernandez, M.A. Cappelli, A 2-D hybrid Hall thruster simulation that resolves the E×B electron drift direction, IEEE Trans. Plasma Sci. **43**, 86 (2015). doi: 10.1109/TPS.2014.2356650

M. Lampe, G. Joyce, W.M. Manheimer, S.P. Slinker, Quasi-neutral particle simulation of magnetized plasma discharges: general formalism and application to ECR discharges, IEEE Trans. Plasma Science **26**, 1592 (1998). doi : 10.1109/27.747877

LANDMARK https://www.landmark-plasma.com/. Access 3 Feb 2019

V. Latocha, L. Garrigues, P. Degond, and J.P. Boeuf, Numerical simulation of electron transport in the channel region of a stationary plasma thruster, Plasma Sources Sci. Technol. **11**, 104 (2002). doi: 10.1088/0963-0252/11/1/313

I. Levchenko, K. Bazaka, Y. Ding, Y. Raitses, S. Mazouffre, T. Henning, P. J. Klar, S. Shinohara, J. Schein, L. Garrigues, M. Kim, D. Lev, F. Taccogna, R. W. Boswell, C. Charles, H. Koizumi, S. Yan, C. Scharlemann, M. Keidar, S. Xu, Space micro-propulsion systems for cubesats and small satellites: from proximate targets to furthermost frontiers, Appl. Phys. Rev. **5**, 011104 (2018). doi: 10.1063/1.5007734

J.A. Linnell, A.D. Gallimore, Internal plasma potential measurements of a Hall thruster using plasma lens focusing, Phys. Plasmas **13**, 103504 (2006). doi: 10.1063/1.2358331

H. Liu, D.R. Yu, G.J. Yan, J.Y. Liu, Investigation of the start transient in a Hall thruster, Contrib. Plasma Phys. **48**, 603 (2008). doi: 10.1002/ctpp.200810094

K.F. Lüskow, P.R.C. Neumann, G. Bandelow, J. Duras, D. Kahnfeld, S. Kemnitz, P. Matthias, K. Matyash, R. Schneider, Particle-in-cell simulation of the cathodic arc thruster, Phys. Plasmas **25**, 013508 (2018). doi: 10.1063/1.5012584

K. Matyash, R. Schneider, A. Mutzke, O. Kalentev, F. Taccogna, N. Koch, M. Scirra, Kinetic simulations of SPT and HEMP thrusters including the near-field plume region, IEEE Trans. Plasma Sci. **38**, 2274-2280 (2010). doi: 10.1109/TPS.2010.2056936

K. Matyash, R. Schneider, S. Mazouffre, S. Tsikata, L. Grimaud, Investigation of rotating spoke instabilities in a wall-less Hall thruster. Part II: Simulation, 35th International Electric Propulsion Conference (The Electric Rocket Propulsion Society, Atlanta, GE), paper no IEPC-2017-403 (2017)

S. Mazouffre, Laser-induced fluorescence diagnostics of the cross-field discharge of Hall thrusters, Plasma Sources Sci. Technol. **22**, 013001 (2013). doi: 10.1088/0963-0252/22/1/013001

S. Mazouffre, Electric propulsion for satellites and spacecraft: established technologies and novel approaches, Plasma Sources Sci. Technol. **25**, 033002 (2016). doi: 10.1088/0963-0252/25/3/033002

S. Mazouffre, L. Grimaud, S. Tsikata, K. Matyash, R. Schneider, Investigation of rotating spoke instabilities in a wall-less Hall thruster. Part I: Experiments, 35th International Electric Propulsion Conference (The Electric Rocket Propulsion Society, Atlanta, GE) paper no IEPC-2017-248 (2017)

N.B. Meezan, M.A. Cappelli, Kinetic study of wall collisions in a coaxial Hall discharge, Phys. Rev. E **66**, 036401 (2002). doi: 10.1103/PhysRevE.66.036401

M Merino, J Mauriño, E. Ahedo, Kinetic electron model for plasma thruster plumes, Plasma Sources Sci. Technol. **27**, 035013 (2018). doi: 10.1088/1361-6595/aab3a1

J. Miedzik, S. Barral, D. Daniłko, Influence of oblique magnetic field on electron cross-field transport in a Hall effect thruster, Phys. Plasmas **22**, 043511 (2015). doi: 10.1063/1.4917079

I.G. Mikellides, I. Katz, Numerical simulations of Hall-effect plasma accelerators on a magnetic-field-aligned mesh, Phys. Rev. E **86**, 046703 (2012). doi:10.1103/PhysRevE.86.046703

I.G. Mikellides, I. Katz, R.R. Hofer, D.M. Goebel, Magnetic shielding of walls from the unmagnetized ion beam in a Hall thruster, Appl. Phys. Lett. **102**, 023509 (2013). doi: 10.1063/1.4776192

I.G. Mikellides, I. Katz, R.R. Hofer, D.M. Goebel, Magnetic shielding of a laboratory Hall thruster. I. Theory and validation, J. Appl. Phys. **115**, 043303 (2014a). doi: 10.1063/1.4862313

I.G. Mikellides, I. Katz, R.R. Hofer, D.M. Goebel, Magnetic shielding of Hall thrusters at high discharge voltages, J. Appl. Phys. **116**, 053302 (2014b). doi: 10.1063/1.4892160

I.G. Mikellides, A.L. Ortega, I. Katz, B.A. Jorns, Hall2De simulations with a first principles electron transport model based on the electron cyclotron drift instability, 52nd Joint AIAA/ASME/SAE/ASEE Propulsion Conference and Exhibit (American Institute of Aeronautics and Astronautics, Salt-Lake City, UT) AIAA paper 2016-4618 (2016)

P. Minelli, F. Taccogna, How to build PIC-MCC models for Hall microthrusters, IEEE Trans. Plasma Science **46**, 219 (2018). doi: 10.1109/TPS.2017.2766182

A.I. Morozov, V.V. Savelyev, One-Dimensional hybrid model of a stationary plasma Thruster, Plasma Phys. Reports **26**, 875 (2000a). doi: 10.1134/1.1316827

A.I. Morozov, V.V. Savelyev, Fundamentals of stationary plasma Thruster theory. In: Kadomtsev B.B., Shafranov V.D. (eds) Reviews of Plasma Physics. Reviews of Plasma Physics, vol 21. Springer, Boston, MA (2000b)

A.I. Morozov, V.V. Savelyev, Theory of the near-wall Conductivity, Plasma Phys. Rep. **27**, 570 (2001). doi: 10.1134/1.1385435

A.I. Morozov, V.V. Savelyev, One-dimensional model of the Debye layer near a dielectric surface, Plasma Phys. Rep. **28**, 1017 (2002). doi: 10.1134/1.1528232

A.I. Morozov, V.V. Savelyev, Structure of steady-state Debye layers in a low-density plasma near a dielectric surface, Plasma Phys. Rep. **30**, 299 (2004). doi: 10.1134/1.1707151

A.I. Morozov V.V. Savelyev, Kinetics of a low-density plasma near a dielectric surface with account for secondary electron emission, Plasma Phys. Rep. **33**, 20 (2007). doi: 10.1134/S1063780X07010035

A.L. Ortega, M.G. Mikellides, M.J. Sekerak, B.A. Jorns, Plasma simulations in 2-D (r-z) geometry for the assessment of pole erosion in a magnetically shielded Hall thruster, J. Appl. Phys. **125**, 033302 (2019). doi: 10.1063/1.5077097

N. Oudini, F. Taccogna, P. Minelli, 3D fully kinetic simulation of near-field plume region, 33rd International Electric Propulsion Conference (The Electric Rocket Propulsion Society, Washington, DC) paper no. IEPC-2013-419 (2013)

F.I. Parra, E. Ahedo, Fulfillment of the Bohm condition on the 'HP Hall' fluid-PIC code, 40th Joint AIAA/ASME/SAE/ASEE Propulsion Conference and Exhibit (American Institute of Aeronautics and Astronautics, Fort-Lauderdale, FL, 2004) AIAA paper 2004-3955 (2004)

F.I. Parra, E. Ahedo, J.M. Fife, M. Martínez-Sánchez, A two-dimensional hybrid model of the Hall thruster discharge, J. Appl. Phys. **100**, 023304 (2006). doi: 10.1063/1.2219165

J. Pérez-Luna, G.J.M. Hagelaar, L. Garrigues, J.P. Boeuf, Method to obtain the electric field and the ionization frequency from laser induced fluorescence measurements, Plasma Sources Sci. Technol. **18**, 034008 (2009). doi: 10.1088/0963-0252/18/3/034008

PETSC, Portable, extensible toolkit for scientific computation, http://www.mcs.anl.gov/petsc

S. Qing, E. Peng, G. Xia, M.C. Tang, P. Duan, Optimized electrode placement along the channel of a Hall thruster for ion focusing, J. Appl. Phys. **115**, 033301 (2014); doi: 10.1063/1.4862299

M. Reza, F. Faraji, T. Andreussi, M. Andrenucci, Model for turbulence-induced electron transport in Hall thrusters, 35th International Electric Propulsion Conference (The Electric Rocket Propulsion Society, Atlanta, GE) paper no IEPC-2017-367 (2017)

S. Roy, B.P. Pandey, Numerical investigation of a Hall thruster plasma, Phys. Plasmas **9**, 4052 (2002). doi: 10.1063/1.1498261

M.K. Scharfe, C.A. Thomas, D.B. Scharfe, N. Gascon, M.A. Cappelli, E. Fernandez, Shear-based model for electron transport in hybrid Hall thruster simulations, IEEE Trans. Plasma Science **36**, 2058 (2008). doi: 10.1109/TPS.2008.2004364

I. Schweigert, T.S. Burton, G.B. Thompson, S. Langendorf, M.L.R. Walker, M. Keidar, Plasma interaction with emissive surface with Debye-scale grooves, Plasma Sources Sci. Technol. **27**, 045004 (2018). doi: 10.1088/1361-6595/aab6d8

M.J. Sekarak, B.W. Longmier, A.D. Gallimore, D.L. Brown, R.R. Hofer, J.E. Polk, Azimuthal spoke propagation in Hall effect thrusters, IEEE Trans. Plasma Science **43**, 72 (2015). doi: 10.1109/TPS.2014.2355223

M.J. Sekarak, B.W. Longmier, A.D. Gallimore, D.L. Brown, R.R. Hofer, J.E. Polk, Mode transitions in Hall-effect thrusters induced by variable magnetic field strength, J. Propul. Power **32**, 903 (2016). doi: 10.2514/1.B35709

A. Shagayda, Stationary electron velocity distribution function in crossed electric and magnetic fields with collisions, Phys. Plasmas **19**, 083503 (2012). doi: 10.1063/1.4744971

A. Shagayda, A. Tarasov, Analytic non-Maxwellian electron velocity distribution function in a Hall discharge plasma, Phys. Plasmas **24**, 103517 (2017). doi: 10.1063/1.5006812

A.W. Smith, M.A. Cappelli, On the role of fluctuations, cathode placement, and collisions on the transport of electrons in the near-field of Hall thrusters, Phys. Plasmas **17**, 093501 (2010). doi: 10.1063/1.3479827

A.W. Smith, M.A. Cappelli, Single particle simulations of electron transport in the near-field of Hall thrusters, J. Phys. D: Appl. Phys. **43**, 045203 (2010). doi: 10.1088/0022-3727/43/4/045203

R. Spektor, Computation of two-dimensional electric field from the ion laser induced fluorescence measurements, Phys. Plasmas **17**, 093503 (2010). doi: 10.1063/1.3481772

R. Spektor, K.D. Diamant, E.J. Beiting, Y. Raitses, N.J. Fisch, Laser induced fluorescence measurements of the cylindrical Hall thruster plume, Phys. Plasmas **17**, 093502 (2010). doi: 10.1063/1.3475433

E. Sommier, M.K. Allis, M.A. Cappelli, Wall erosion in 2D Hall thruster simulations, 29th International Electric Propulsion Conference (The Electric Rocket Propulsion Society, Princeton, NJ) paper no IEPC-2005-189 (2005)

T.H. Stix, *The Theory of Plasma Waves* (McGraw-Hill, New York, 1962)

SUPERLU, http://crd-legacy.lbl.gov/~xiaoye/SuperLU/

D. Sydorenko, Particle-in-cell simulations of electron dynamics in low pressure discharges with magnetic fields, Ph.D. thesis, Department of Physics and Engineering Physics, University of Saskatchewan, Saskatoon (2006)

D. Sydorenko, A. Smolyakov, I. Kaganovich, Y. Raitses, Kinetic simulation of secondary electron emission effects in Hall thrusters, Phys. Plasmas **13**, 014501 (2006). doi: 10.1063/1.2158698

D. Sydorenko, A. Smolyakov, I. Kaganovich, Y. Raitses, Effects of non-Maxwellian electron velocity distribution function on two-stream instability in low-pressure discharges, Phys. Plasmas **14**, 013508 (2007). doi: 10.1063/1.2435315

D. Sydorenko, A. Smolyakov, I. Kaganovich, Y. Raitses, Plasma-sheath instability in Hall thrusters due to periodic modulation of the energy of secondary electrons in cyclotron motion, Phys. Plasmas **15**, 053506 (2008). doi: 10.1063/1.2918333

D. Sydorenko, I. Kaganovich, Y. Raitses, A. Smolyakov, Breakdown of a space charge limited regime of a sheath in a weakly collisional plasma bounded by walls with secondary electron emission, Phys. Rev. Lett. **103**, 145004 (2009). doi: 10.1103/PhysRevLett.103.145004

J. Szabo, N. Warner, M. Martinez-Sanchez, O. Batishchev, Full Particle-In-Cell Simulation Methodology for Axisymmetric Hall Effect Thrusters, J. Prop. and Power **30**, 197 (2014). doi: 10.2514/1.B34774

F. Taccogna, S. Longo, M. Capitelli, Particle-in-cell with Monte Carlo simulation of SPT-100 exhaust plumes, J. Spac. and Rock. **39(3)**, 409-419 (2002). doi: 10.2514/2.3840

F. Taccogna, S. Longo, M. Capitelli, R. Schneider, Stationary plasma thruster simulation, Comp. Phys. Comm. **164**, 160 (2004a). doi: 10.1016/j.cpc.2004.06.025

F. Taccogna, S. Longo, M. Capitelli, Very-near-field plume simulation of a stationary plasma thruster, The Europ. Phys. J.-Appl. Phys. **28(1)**, 113-122 (2004b). doi: 10.1051/epjap:2004151

F. Taccogna, S. Longo, M. Capitelli, Plasma sheaths in Hall discharge, Phys. Plasmas **12**, 093506 (2005a). doi: 10.1063/1.2015257

F. Taccogna, S. Longo, M. Capitelli, R. Schneider, Plasma flow in a Hall thruster, Phys. Plasmas **12**, 043502 (2005b). doi: 10.1063/1.1862630

F. Taccogna, S. Longo, M. Capitelli, R. Schneider, Self-similarity in Hall plasma discharges: Applications to particle models, Phys. Plasmas **12**, 053502 (2005c). doi: 10.1063/1.1877517

F. Taccogna, R. Schneider, S. Longo, M. Capitelli, Effect of surface roughness on secondary electron emission in a Hall discharge, 42nd Joint AIAA/ASME/SAE/ASEE Propulsion Conference and Exhibit (American Institute of Aeronautics and Astronautics, Sacramento, CA) AIAA paper 2006-4662 (2006a)

F. Taccogna, S. Longo, M. Capitelli, R. Schneider, Start-up transient in a Hall thruster, Contr. Plasma Phys. **46**, 781 (2006b). doi: 10.1002/ctpp.200610078

F. Taccogna, S. Longo, M. Capitelli, R. Schneider, Particle-in-Cell Simulation of Stationary Plasma Thruster, Contrib. Plasma Phys. **47(8-9)**, 635-656 (2007). doi: 10.1002/ctpp.200710074

F. Taccogna, S. Longo, M. Capitelli, R. Schneider, Kinetic simulations of a plasma thruster, Plasma Sources Sci. Technol. **17**, 024003 (2008). doi: 10.1088/0963-0252/17/2/024003

F. Taccogna, S. Longo, M. Capitelli, R. Schneider, Surface-driven asymmetry and instability in the acceleration region of Hall thruster, Contr. Plasma Phys. **48**, 375 (2008b). doi: 10.1002/ctpp.200810061

F. Taccogna, S. Longo, M. Capitelli, R. Schneider, Anomalous transport induced by sheath instability in Hall effect thrusters, Appl. Phys. Lett. **94**, 251502 (2009). doi: 10.1063/1.3152270

F. Taccogna, S. Longo, M. Capitelli, R. Schneider, On a new mechanism inducing anomalous transport in surface-dominated magnetically confined plasma: the sheath instability, Nuovo Cimento B **125**, 5 (2010). doi : 10.1393/ncb/i2010-10858-6

F. Taccogna, Non-classical plasma sheaths: space-charge-limited and inverse regimes under strong emission from surfaces, The European Physical Journal D **68** 199 (2014a). doi:10.1140/epjd/e2014-50132-5

F. Taccogna, D. Pagano, F. Scortecci, A. Garulli, Three-dimensional plume simulation of multi-channel thruster configuration, Plasma Sources Sci. Technol. **23**, 065034 (2014b). doi: 10.1088/0963-0252/23/6/065034

F. Taccogna, Monte Carlo collision method for low temperature plasma simulation, J. Plasma Phys. **81**, 305810102 (2015). doi: 10.1017/S0022377814000567

F. Taccogna, P. Minelli, Three-dimensional particle-in-cell model of Hall thruster: The discharge channel, Phys. Plasmas **25**, 061208 (2018). doi: 10.1063/1.5023482

F. Taccogna, P. Minelli, Z. Asadi, G. Bogopolsky, Numerical studies of the ExB electron drift instability in Hall thrusters, to appear in Plasma Sources Sci. Technol. (2019)

Y. Takao, H. Koizumi, K. Komurasaki, K. Eriguchi, K. Ono, Three-dimensional particle-in-cell simulation of a miniature plasma source for a microwave discharge ion thruster, Plasma Sources Sci. Technol. **23**, 064004 (2014). doi: 10.1088/0963-0252/23/6/064004

A. Tavant, V. Croes, R. Lucken, T. Lafleur, A. Bourdon, P. Chabert, The effects of secondary electron emission on plasma sheath characteristics and electron transport in an ExB discharge via kinetic simulations, Plasma Sources Sci. Technol. **27**, 124001 (2018). doi: 10.1088/1361-6595/aaeccd

T. Tondu, M. Belhaj, V. Inguimbert, Electron-emission yield under electron impact of ceramics used as channelmaterials in Hall-effect thrusters, J. Appl. Phys. 110, 093301 (2011). doi: :10.1063/1.3653820

M. Touzeau, M. Prioul, S. Roche, N. Gascon, C. Pérot, F. Darnon, S. Béchu, C. Philippe-Kadlec, L. Magne, P. Lasgorceix, D. Pagnon, A. Bouchoule, M. Dudeck, Plasma diagnostic systems for Hall-effect plasma thrusters, Plasma Phys. Control. Fusion **42**, B323 (2000). doi: 10.1088/0741-3335/42/12B/324

S. Tsikata, C. Honoré, N. Lemoine, D.M. Grésillon, Three-dimensional structure of electron density fluctuations in the Hall thruster plasma: ExB mode, Phys. Plasmas **17**, 112110 (2010). doi: 10.1063/1.3499350

M.J.L. Turner, *Rocket and spacecraft propulsion*, Second edition, Chichester, Springer (2009)

J.R.M. Vaughan, A new formula for secondary emission yield, IEEE Trans. Electron. Devices **36**, 1963 (1989). doi: 10.1109/16.34278

M. Villemant, P. Sarrailh, M. Belhaj, C. Inguimbert, L. Garrigues, C. Boniface, Electron emission for Hall thruster plasma modelling, 35th International Electric Propulsion Conference (The Electric Rocket Propulsion Society, Atlanta, GE) paper no IEPC-2017-366 (2017)

H. Wang, M.D. Campanell, I.D. Kaganovich, G. Cai, Effect of asymmetric secondary emission in bounded low-collisional ExB plasma on sheath and plasma properties, J. Phys. D: Appl. Phys. **47**, 405204 (2014). doi:10.1088/0022-3727/47/40/405204

WSMP, Watson sparse matrix package, http://www.research.ibm.com/projects/wsmp

A.P. Yalin, B. Rubin, S.R. Domingue, Z. Glueckert, J.D. Williams, Differential sputter yields of boron nitride, quartz, and kapton due to low energy Xe+ bombardment, 43rd Joint AIAA/ASME/SAE/ASEE Propulsion Conference and Exhibit Cincinnati (American Institute of Aeronautics and Astronautics, OH, 2007) AIAA paper 2007-5314 (2007)

Y. Yamamura, H. Tawara, Energy dependence of ion-induced sputtering yields from monatomic solids at normal incidence, At. Data Nucl. Data Tables **62**, 149 (1996). doi: 10.1006/adnd.1996.0005; Erratum, At. Data Nucl. Data Tables **63**, 353 (1996), doi: 10.1006/adnd.1996.0016

J. Yang, S. Yokota, R. Kaneko, K. Komurasaki, Diagnosing on plasma plume from xenon Hall thruster with collisional-radiative model, Phys. Plasmas **17**, 103504 (2010). doi: 10.1063/1.3486530

J.T Yim, M. Keidar, I.D. Boyd, An investigation of factors involved in Hall thruster wall erosion modeling, 42nd Joint AIAA/ASME/SAE/ASEE Propulsion Conference and Exhibit (American Institute of Aeronautics and Astronautics, CA, 2006) AIAA paper 2006-4657 (2006)

D. Yu, Y. Li, Volumetric erosion rate reduction of Hall thruster channel wall during ion sputtering process, J. Phys. D: Appl. Phys. **40**, 2526 (2007). doi: 10.1088/0022-3727/40/8/017

D.R. Yu, S.W. Qing, H. Liu, H. Li, Particle-in-cell simulation for the effect of segmented electrodes near the exit of an Aton-type Hall thruster on ion focusing acceleration, Contrib. Plasma Phys. **51**, 955 (2011). doi: 10.1002/ctpp.201100036

D. Yu, M. Song, H. Liu, Y.J. Ding, H. Li, Particle-in-cell simulation of a double stage Hall thruster, Phys. Plasmas **19**, 033503 (2012). doi: 10.1063/1.3688903

F. Zhang, D. Yu, Y. Ding, H. Li, The spatiotemporal oscillation characteristics of the dielectric wall sheath in stationary plasma thrusters, Appl. Phys. Lett. **98**, 111501 (2011). doi: 10.1063/1.3564898

F. Zhang, L. Kong, X. Zhang, W. Li, D. Yu, Effect of electron temperature anisotropy on near-wall conductivity in Hall thrusters, Phys. Plasmas **21**, 060703 (2014). doi: 10.1063/1.4885358

V.V. Zhurin, H.R. Kaufman, R.S. Robinson, Physics of closed drift thrusters, Plasma Sources Sci. Technol. **8**, R1 (1999). doi: 10.1088/0963-0252/8/1/021

Affiliations

F. Taccogna[1] · L. Garrigues[2]

L. Garrigues

laurent.garrigues@laplace.univ-tlse.fr

[1] PLasMI research group @ CNR-Nanotec, 70126 Bari, Italy

[2] LAPLACE, Université de Toulouse, CNRS, INPT, UPS, 31062 Toulouse, France